An efficient semi-analytical framework to tailor snap-through loads in bistable variable stiffness laminates

Ayan Haldar[a,*], R.M.J. Groh[b], Eelco Jansen[a], Paul M. Weaver[b,c], Raimund Rolfes[a]

[a]*Institute of Structural Analysis, Leibniz Universität Hannover, Appelstrasse 9A, 30167 Hannover, Germany*
[b]*Bristol Composites Institute (ACCIS), Department of Aerospace Engineering, University of Bristol, Queen's Building, University Walk, BS8 1TR, Bristol, UK*
[c]*Bernal Institute, School of Engineering, University of Limerick, Castletroy, Ireland*

Abstract

Multistable laminates are potential candidates for adaptive structures due to the existence of multiple stable states. Commonly, such bistable shapes are generated from the cool-down process of the unsymmetric laminates from the curing temperature. In this work, we exploit unsymmetric variable stiffness laminates with curvilinear fiber paths to generate similar bistable shapes as unsymmetric cross-ply laminates, but with the possibility to tailor the snap-through loads. Snap-through is a complex phenomenon in that is difficult to characterize using simple analytical models. An accurate yet computationally efficient semi-analytical model is proposed to compute the snap-through forces of bistable variable stiffness (VS) laminates. The differential equations resulting from the compatibility and the in-plane equilibrium equations are solved with negligible numerical error using the Differential Quadrature Method (DQM). As a result, the in-plane stress resultants and the total potential energy is written in terms of curvatures. The out-of-plane displacements are expressed in the form of Legendre polynomials where the unknown coefficients of the displacement function are found using the Rayleigh-Ritz formulation. The calculated

*Corresponding author
Email address: `a.haldar@isd.uni-hannover.de` (Ayan Haldar)

snap-through loads are then compared with the Finite Element (FE) results. A parametric study is conducted to explore the tailoring capabilities of VS laminates for snap-through loads.
Keywords: Multistability, Variable stiffness composites, Nonlinear plates, Rayleigh Ritz, Snap-through loads, Residual thermal stresses, Differential quadrature method

---

1. Introduction

In the aerospace industry, shape changing capabilities offer significant improvement in performance, as compared with fixed geometry and can efficiently meet different operational requirements. In the recent past, multistable structures have shown great potential in morphing applications [1, 2, 3, 4, 5, 6, 7], especially due to the existence of multiple stable shapes and the ability to remain in these stable states without any external forces.

Multistable structures can be generated either by utilizing the differential thermal coefficient of an unsymmetric laminate in orthogonal directions [8], or as a result of tuning the geometry such as changing Gaussian curvature in initially curved shells [9], controlling slit spacing in kirigami-inspired structure [10] or due to prestressing [11]. However, thermally induced bistable shapes of unsymmetric laminates often result in a narrow range of shapes limiting its use in different applications. Haldar et al. [12] observed that variable stiffness (VS) laminates could be used to generate a wider range of stable shapes than that of constant stiffness laminates. Panesar et al. [13, 14] employed a bistable tow-steered blended laminate to study a morphing trailing edge flap and also found the optimum fiber direction for maximum out-of-plane displacement and angle of attack.

A cylindrical bistable configuration without any twisting curvature is typically constructed from $[0_n/90_n]$ unsymmetrical laminate. A similar stable shape can be also be generated using different options of VS configurations [12, 60]. One such example of VS laminate exhibiting similar cylindrical bistable shape as $[0_n/90_n]$ unsymmetrical laminate is shown in Figure 1.

Snapping in a bistable shell structure is a complex phenomenon, which is determined by the interplay between bending and stretching energies. Several methods have so far been proposed to snap from one stable shape to another, for example by using external forces [15, 16], electric current [17], magnetic actuators [18, 19] or induced curvature due to non-mechanical stimuli like temperature and swelling [20, 21]. It has been shown previously that both initial curvature and material parameters are two important attributes dictating the snapping process [22, 23]. Due to their vast augmented design space, VS laminates offer tremendous freedom to tailor material parameters in such a way that the snapping behavior can be controlled. Thus, in this work, we exploit and study the dependence of the fiber angle parameters defining curvilinear fiber orientation on the snap-through loads. It has been previously reported in Diaconu et al. [24], that even for constant fiber angle laminates, the uniform curvature assumption fails to predict snap-through loads accurately, as the snapping process involves intermediate non-cylindrical shapes. The same was observed experimentally by Potter et al. [25]. Higher-order displacement fields are therefore necessary to capture the complex phenomenon of the snap-through event. However, as observed by Mattioni et al. [26] and Pirrera et al. [15], with such approximations, the in-plane displacement and strain field expressions lead to high computational costs. Nonlinear finite element (FE) analysis proves to be an accurate predictive tool, but the high computational cost may not be suitable for optimization or parametric studies. Therefore, a fast and sufficiently accurate analytical tool is required to study the snap-through behavior of VS laminates.

Lamacchia et al. [27] showed that the Differential Quadrature Method (DQM) proves to be a computationally efficient and robust framework to capture the snap-through behavior of constant fiber laminates. The key to this formulation is to decouple the bending and stretching parts of the total strain energy, using a semi-inverse constitutive relation. As suggested by Vidoli et al. [28], it is crucial to solve the membrane problem with negligible numerical error to evaluate the stretching energy accurately. To reduce the number of unknowns in Lamacchia et al. [27], the in-plane stress resultants are expressed once and for all in terms of curvatures and thermal strains using the compatibility equation and the constitutive relations. The total energy is then expressed as a function of just curvatures and thermal strains. Here we extend the formulation by Lamacchia et al. [27] and preliminary work done by Haldar et al. [29] for VS laminates and derive a computationally efficient and robust technique to calculate snap-through forces in these laminates.

Snap-through is triggered by applying four concentrated forces at the corners of a square plate. The contribution of the external forces is subsequently added to the total energy of the system. Equilibrium states are then found by minimizing the total energy. The Hessian of the total potential energy with respect to the unknown coefficients of the out-of-plane displacement field indicates if the solution is stable or unstable. The developed model is subsequently compared with FE results. A parametric study is further conducted to explore the design regimes of VS laminates leading to lower snap-through loads but still retaining a similar cool-down shape as a cross-ply laminate.

The novelty of the work revolves particularly around two points. Firstly, a computationally efficient analytical model is developed to calculate the snap-through forces for VS laminates in a reasonably accurate way. This model also helps us to understand the different snap-through modes in VS laminates. Secondly, the model is used for the first time to analyze out-of-plane displacements and snap-through loads for a family of VS-laminates generating similar cylindrical bistable shapes that were until now only possible by using an unsymmetrical $[0_n/90_n]$ layup.

The paper is organized into the following sections. Section 2 describes the adopted curvilinear fiber trajectory, defining the necessary fiber angle parameters. The following Section 3 describes briefly the adopted methodology followed by its non-dimensional form in Section 4. The so-called membrane problem, where the in-plane stresses are calculated numerically using DQM, is described in Section 5. Section 6 describes the results obtained from the analytical model which are compared with the results obtained from the FE model. The snap-through loads, as well as the out-of-plane displacements, are calculated in a parametric study described in Section 7 for the family of VS laminates, whose cylindrical bistable shapes are similar to those obtained from unsymmetric cross-ply laminates. Finally, concluding remarks can be found in Section 9.

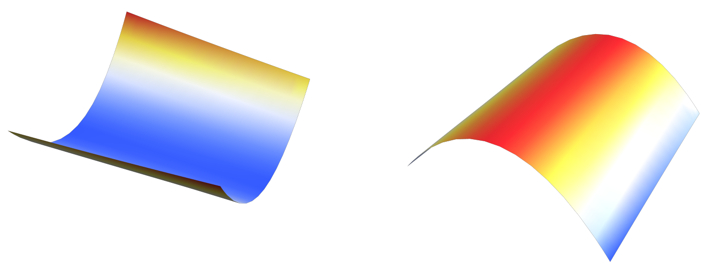

(a) **(b)**

Figure 1: Example of bistable shapes generated from an unsymmetric VS laminate $[45\langle 30|60\rangle_4/45\langle -30|-60\rangle_4]_T$. The bistable shapes are similar to that obtained from unsymmetric cross ply laminates.

2. Variable stiffness model

With the advent of new fiber placement technologies [30, 31, 32, 33], spatial variation in the fiber orientation angle can be achieved by placing the fiber in a curvilinear fashion within the plane of each composite lamina. A considerable amount of work has been carried out about the mechanical behaviour of composite laminates with variable fiber orientations. The initial idea of introducing curvilinear fibers was proposed by Hyer et al. [34, 35], where a laminated square plate with a central circular hole was investigated using curvilinear fiber paths. Gürdal and Olmedo [36] adopted a linear variation of fiber paths, and showed significant improvements in the buckling performance by stiffness tailoring using curvilinear fibers. Later, Gürdal [37] also adopted fiber trajectories with constant curvature based on the definition of circular arcs.

Nonlinear variations of fiber angle have also been adopted by several researchers to enhance the design space, for example using Lagrange polynomials [38, 39, 40], Bezier curves [41], B-Splines [42, 43] and Lobatto polynomial [44, 45]. However, manufacturability constraints should be considered for any proposed fiber path, to avoid fiber breakage and wrinkling when steering with a small curvature radius. Some recent works have elucidated the effect of manufacturing constraints on optimal designs of VS laminates [46, 47, 48].

The simple model with a linear variation of fiber angle is widely adopted in several works, and has led to manufacturable results. In this paper, the bilinear fiber variation proposed by Gürdal et al. [49] is extended to a smoother nonlinear fiber variation at the centroid of the laminate as shown in Figure 2. The original linear variation by Gürdal et al. [49] imposed a symmetric fiber path around the centroid of the laminate, which led to a non-differentiable function at this point. A smoother transition can obviate numerical errors pertaining to differentiation of the fiber orientation angle θ near the center of the plate.

The fiber orientation angle θ for the reference fiber path is defined as follows:

$$\theta(x') = \phi + \frac{(T_1 - T_0)}{d}\frac{a|x'|^3}{1 + a(x')^2} + T_0 \tag{1}$$

where

$$x' = x\cos\phi + y\sin\phi. \tag{2}$$

Figure 3 illustrates different paramaters defining the VS laminate. The angle parameter T_0 refers to the fiber orientation angle at the centroid of the plate (point A) whereas T_1 refers to the angle at the length d of the plate (point B). The length d is referred as the "characteristic length". The parameter ϕ is the angle at which the fiber coordinate system is inclined with the global Cartesian coordinate system. The other fiber trajectories are constructed by shifting the reference fiber path in the direction perpendicular to the x' axis. The standard notation to define a particular VS laminate with the abovementioned three parameters is as follows: $\phi\langle T_0|T_1\rangle$.

In comparison to the linearly varying fiber angle in the model introduced by Gürdal et al. [49], an additional parameter a is introduced, which adds nonlinearity to the variation of fiber orientation angle at the center of the plate.

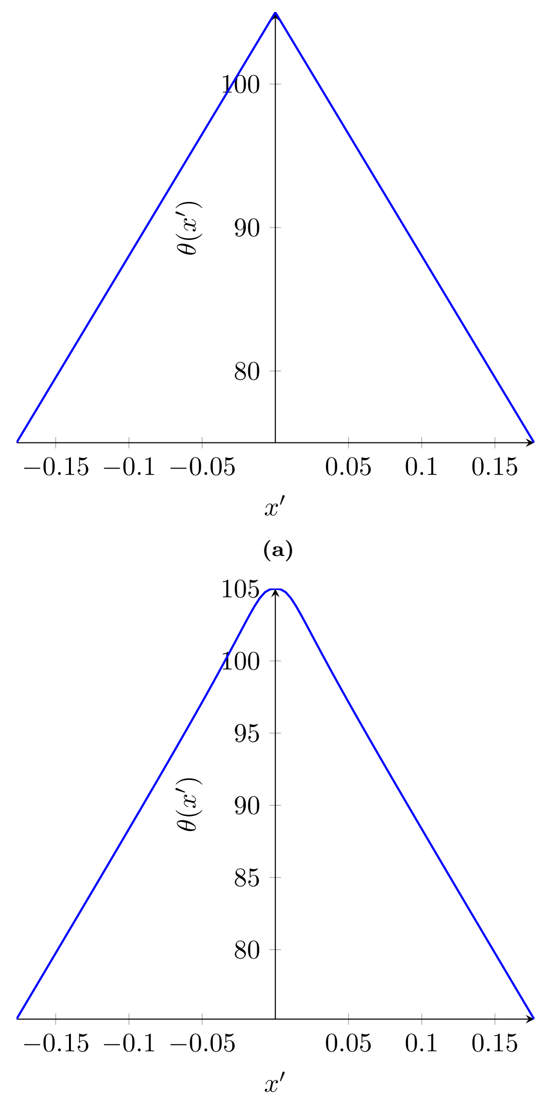

(a)

(b)

Figure 2: Variation of fiber angle for $[45\langle 15|75\rangle]$ a) Bilinear Variation ([49]), b) Nonlinear Variation with $a = 1000$

Therefore, the fiber angle variation defined here is similar to the typical linear variation but with a smoother nonlinear transition of fiber angle at the center of the plate.

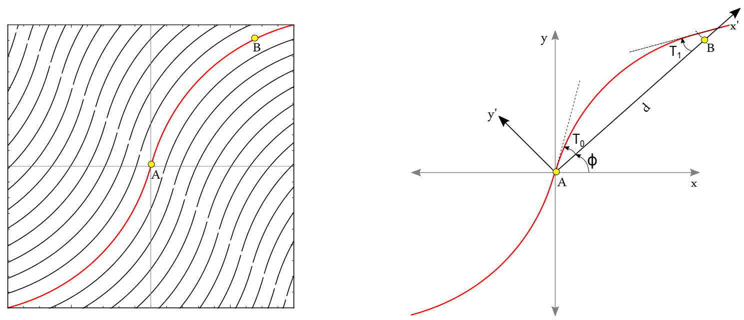

Figure 3: Parameters defining the curvilinear fiber path ([49])

3. Theoretical Development

3.1. Kinematics

A material point in the deformed configuration can be expressed as $\mathbf{x} = \mathbf{X} + \mathbf{u}$, where $\mathbf{u}(u, v, w)$ denotes the displacement vector in the x, y and z direction, whereas $\mathbf{x}$, $\mathbf{X}$ identify the position vectors in the deformed and in the undeformed reference configuration, respectively. The components of the displacement vector are defined as [50]:

$$u(x, y, z) = u_0(x, y) - z\frac{\partial w_0}{\partial x}, \quad v(x, y, z) = v_0(x, y) - z\frac{\partial w_0}{\partial y}, \quad w(x, y, z) = w_0(x, y) \ , \tag{3}$$

where the subscript 0 identifies the mid-plane displacements.

The strain components include nonlinear von Kármán strains under the assumption of small strains and moderate rotations and are given by:

$$\epsilon_{xx} = \frac{\partial u}{\partial x} + \frac{1}{2}\left(\frac{\partial w}{\partial x}\right)^2, \quad \epsilon_{yy} = \frac{\partial v}{\partial y} + \frac{1}{2}\left(\frac{\partial w}{\partial y}\right)^2, \quad \gamma_{xy} = \frac{\partial u}{\partial y} + \frac{\partial v}{\partial x} + \frac{\partial w}{\partial x}\frac{\partial w}{\partial y} \tag{4}$$

which shows the nonlinear strain-displacement relationships. By inserting Eq.

(3) into Eq. (4), the strain relations can be rearranged as:

$$\boldsymbol{\epsilon}=\begin{bmatrix}\epsilon_{xx}\\ \epsilon_{yy}\\ \gamma_{xy}\end{bmatrix}=\begin{bmatrix}\varepsilon_{xx}\\ \varepsilon_{yy}\\ \varepsilon_{xy}\end{bmatrix}+z\begin{bmatrix}\kappa_{xx}\\ \kappa_{yy}\\ \kappa_{xy}\end{bmatrix}=\begin{bmatrix}\frac{\partial u_0}{\partial x}+\frac{1}{2}\left(\frac{\partial w_0}{\partial x}\right)^2\\ \frac{\partial v_0}{\partial y}+\frac{1}{2}\left(\frac{\partial w_0}{\partial y}\right)^2\\ \frac{\partial u_0}{\partial y}+\frac{\partial v_0}{\partial x}+\frac{\partial w_0}{\partial x}\frac{\partial w_0}{\partial y}\end{bmatrix}+z\begin{bmatrix}-\frac{\partial^2 w_0}{\partial x^2}\\ -\frac{\partial^2 w_0}{\partial y^2}\\ -2\frac{\partial^2 w_0}{\partial x\partial y}\end{bmatrix}=\boldsymbol{\varepsilon}+z\boldsymbol{\kappa}, \tag{5}$$

where $\boldsymbol{\varepsilon}$ and $\boldsymbol{\kappa}$ represent the mid-plane strain and curvature vectors, respectively.

3.2. Calculation of total energy

The total strain energy can be written as:

$$\mathit{\Pi}=\frac{1}{2}\int_S\left[\boldsymbol{\varepsilon}^T\boldsymbol{A}(x,y)\boldsymbol{\varepsilon}\right]dS+\int_S\left[\boldsymbol{\varepsilon}^T\boldsymbol{B}(x,y)\boldsymbol{\kappa}\right]dS+\frac{1}{2}\int_S\left[\boldsymbol{\kappa}\boldsymbol{D}(x,y)\boldsymbol{\kappa}\right]dS-\int_S\boldsymbol{N}^{th}\boldsymbol{\varepsilon}dS-\int_S\boldsymbol{M}^{th}\boldsymbol{\kappa}dS\ , \tag{6}$$

where the superscript ^{T} denotes vector transpose, N^{th} and M^{th} represent stresses and moments associated with thermal effects, respectively and dS refers to the surface element. It should also be noted that as the fiber orientation is a function of x and y, the **ABD** matrix also varies with the coordinates of the plate. This flexibility to change the stiffness terms of the plate as a function of the coordinates of the composite gives the designer a wide range of tailoring possibilities. Using the semi-inverse constitutive relations, the strains can be written in terms of curvatures and stress resultants as follows:

$$\boldsymbol{\varepsilon}=\boldsymbol{A}^*(\boldsymbol{N}+\boldsymbol{N}^{th})+\boldsymbol{B}^*\boldsymbol{\kappa}\ . \tag{7}$$

The bending and the membrane part of total strain energy can then be decoupled and written as:

$$\begin{aligned}\mathit{\Pi}=&\overbrace{\frac{1}{2}\int_S\left[\boldsymbol{N}^T\boldsymbol{A}^*(x,y)\boldsymbol{N}\right]dS}^{\text{Membrane Energy}}+\overbrace{\frac{1}{2}\int_S\left[\boldsymbol{\kappa}^T\boldsymbol{D}^*(x,y)\kappa\right]dS}^{\text{Bending Energy}}\\ &-\frac{1}{2}\int_S\left[(\boldsymbol{N}^{th})^T\boldsymbol{A}^*(x,y)\boldsymbol{N}^{th}\right]dS-\int_S\left[(\boldsymbol{N}^{th})^T\boldsymbol{B}^*(x,y)\boldsymbol{\kappa}\right]dS\\ &-\int_S\left[(\boldsymbol{M}^{th})^T\boldsymbol{I}\boldsymbol{\kappa}\right]dS\ ,\end{aligned} \tag{8}$$

with

$$\begin{aligned}
\boldsymbol{A}^* &:= \boldsymbol{A}^{-1} \\
\boldsymbol{B}^* &:= -\boldsymbol{A}^{-1}\boldsymbol{B} \\
\boldsymbol{D}^* &:= \boldsymbol{D} - \boldsymbol{B}^T\boldsymbol{A}^{-1}\boldsymbol{B} \, ,
\end{aligned} \tag{9}$$

where I is the unit matrix. $\boldsymbol{N}$ and $\boldsymbol{M}$ are the vectors containing the resultant forces and moments respectively. This formulation as shown by Lamacchia et al. [27] clearly reveals the independent contribution of bending and stretching parts of the total strain energy. The minimization of Eq. 8 reveals the equilibria in the admissible space of in-plane and out-of-plane displacements.

3.3. Membrane Problem

Compatibility of a shallow shell relates the in-plane strains and the curvatures[51, 52].

$$\mathcal{L}_A(\boldsymbol{\varepsilon}) = \frac{\partial^2 \varepsilon_{yy}}{\partial x^2} + \frac{\partial^2 \varepsilon_{xx}}{\partial y^2} - \frac{\partial^2 \varepsilon_{xy}}{\partial x \partial y} = \det \kappa = \kappa_{xx}\kappa_{yy} - \kappa_{xy}^2/4 \, , \tag{10}$$

where $\det \kappa$ denotes the Gaussian curvature. Note that the plate studied in this work is initially flat and therefore the value of initial curvature is considered to be zero. The in-plane equilibirum equation can be written as:

$$\mathrm{div}\boldsymbol{N} = 0 \quad \text{on } S, \qquad \boldsymbol{N}.\boldsymbol{n} = 0 \quad \text{on } \partial S \, , \tag{11}$$

where $\boldsymbol{n}$ refers to the normal of the plate and ∂S refers to its boundary. By combining both the compatibility Eq. 10 and the in-plane equilibrium Eq. 11, the in-plane stress resultants can be expressed in terms of the curvatures, without the need to introduce separate polynomial functions for the membrane problem. From the semi-constitutive relation in Eq. 7, the in-plane strains can be written in terms of stresses and curvatures as:

$$\mathcal{L}_A(\boldsymbol{A}^*\boldsymbol{N}) = \det\boldsymbol{\kappa} - \mathcal{L}_A\left(\boldsymbol{A}^*\boldsymbol{N}^{th} + \boldsymbol{B}^*\boldsymbol{\kappa}\right) := f \quad \text{on } S \, , \tag{12}$$

where the term $\mathcal{L}_A(\boldsymbol{A}^*\boldsymbol{N}^{th} + \boldsymbol{B}^*\boldsymbol{\kappa})$ is non-zero for VS laminates.

It is important therefore to solve the set of differential equations accurately, with a good estimation of the in-plane stress resultants. The importance of reducing the degrees of freedom by solving the membrane problem only once, was previously shown by Vidoli [28] and Lamacchia et al. [27]. The membrane problem can be solved by applying DQM to Eq. 11 and Eq. 12, where the individual terms are converted into DQM matrices of weighting coefficients, which are solved over a Chebyshev-Gauss-Lobatto mesh grid.

4. Non-Dimensional Form

4.1. Formulation

To minimise the ill-conditioning of the nonlinear model, a non-dimensionalisation procedure is performed, with ($\sim$) representing the non-dimensionalised form. In this section, all the components are defined in the dimensionless form. The coordinate axis is defined as $x = L_x\tilde{x}$ and $y = L_y\tilde{y}$ and therefore the displacement vectors are:

$$u = U_d\tilde{u}, v = V_d\tilde{v}, w = W_d\tilde{w} \,. \tag{13}$$

Further, the strain components can therefore be written in dimensionless quantities as:

$$\boldsymbol{\varepsilon} = \boldsymbol{E}\tilde{\boldsymbol{\varepsilon}}, \boldsymbol{\kappa} = \boldsymbol{K}\tilde{\boldsymbol{\kappa}} \,, \tag{14}$$

where:

- $2L_x$ and $2L_y$ are the side lengths of the plate along the Cartesian axes,
- U_d, V_d, W_d are defined as [15, 27] :

$$\begin{aligned} U_d &= \frac{1}{L_x}\sqrt{A^*_{11}A^*_{22}D^*_{11}D^*_{22}} \\ V_d &= \frac{1}{L_y}\sqrt{A^*_{11}A^*_{22}D^*_{11}D^*_{22}} \\ W_d &= \sqrt[4]{A^*_{11}A^*_{22}D^*_{11}D^*_{22}} \end{aligned} \tag{15}$$

- The in-plane strains and curvatures can be scaled using $\mathbf{E}$ and $\mathbf{K}$, as given below:

$$
\begin{aligned}
E_{xx} = \quad & \frac{1}{2}\frac{W_d^2}{L_x^2}, E_{yy} = \quad \frac{1}{2}\frac{W_d^2}{L_y^2}, E_{xy} = \quad \frac{W_d^2}{L_x L_y} \\
K_{xx} = \quad & -\frac{W_d}{L_x^2}, K_{yy} = \quad -\frac{W_d}{L_y^2}, K_{xy} = \quad -2\frac{W_d}{L_x L_y}
\end{aligned}
\tag{16}
$$

The thermal forces and the moments can be scaled as: $\boldsymbol{N}^{th} = \tilde{\boldsymbol{N}}^{th}\tilde{\tau}$ and $\boldsymbol{M}^{th} = \tilde{\boldsymbol{M}}^{th}\tilde{\tau}$. Here, $\tilde{\tau}$ is defined as:

$$
T - T_{ref} = \Delta T_0 \tilde{\tau} \,, \tag{17}
$$

where T to the current temperature, T_{ref} is the curing temperature and ΔT_0 is the difference between curing and room temperature. The thermal force resultants $\tilde{\boldsymbol{N}}^{th}$ and the moment results $\tilde{\boldsymbol{M}}^{th}$ can be written as:

$$
\begin{aligned}
\tilde{\boldsymbol{N}}^{th} &= \sum_{k=1}^{n_{ply}} \int_{z_k}^{z_{k+1}} \boldsymbol{Q}_k\left(x,y\right) \boldsymbol{\alpha}_k\left(x,y\right) \Delta T dz \\
\tilde{\boldsymbol{M}}^{th} &= \sum_{k=1}^{n_{ply}} \int_{z_k}^{z_{k+1}} \boldsymbol{Q}_k\left(x,y\right) \boldsymbol{\alpha}_k\left(x,y\right) \Delta T z dz \,.
\end{aligned}
\tag{18}
$$

$\boldsymbol{Q}_k$ refers to the reduced stiffness matrix whereas $\boldsymbol{\alpha}_k$ corresponds to the coefficient of thermal expansion transformed in the laminate coordinate for the k^{th} layer.

Legendre polynomials are used to describe the out-of-plane displacements w, from which the curvature fields are calculated. The following definition of w is used:

$$
\tilde{w}(x,y) = \tilde{w}_0(x,y) + \sum_{i=0}^{n}\sum_{j=0}^{n} q_{ij} P_i(x) Q_j(y) \,, \tag{19}
$$

where $\tilde{w}_0$ is the dimensionless out-of-plane displacement at the mid-plane surface and $P_i(x)$ and $Q_j(y)$ are defined as:

$$
\begin{aligned}
P_i(x) &= \sum_{k=0}^{l} \binom{l}{k} \binom{-l-1}{k} \left(\frac{1-x}{2}\right)^k \,, \\
Q_j(y) &= \sum_{k=0}^{l} \binom{l}{k} \binom{-l-1}{k} \left(\frac{1-y}{2}\right)^k \,.
\end{aligned}
\tag{20}
$$

For a $2n$-order polynomial, there are $(n+1)^2$ different combinations of shape functions $P_i(x)Q_j(y)$ multiplied with q_{ij} unknown parameters. With this approximation of the out-of-plane displacement $\tilde{w}$, the membrane problem is re-written in dimensionless form, where the in-plane stresses resultants can be expressed in terms of the unknown coefficients q_{ij} defining $\tilde{w}$.

4.2. Compatibility Equation

The compatibility equation in the non-dimensional form reads as:

$$\frac{1}{2}\frac{\partial^2 \tilde{\varepsilon}_{yy}}{\partial \tilde{x}^2} + \frac{1}{2}\frac{\partial^2 \tilde{\varepsilon}_{xx}}{\partial \tilde{y}^2} - \frac{\partial^2 \tilde{\varepsilon}_{xy}}{\partial \tilde{x}\partial \tilde{y}} = \det \tilde{\kappa} = \tilde{\kappa}_{xx}\tilde{\kappa}_{yy} - \tilde{\kappa}_{xy}^2. \tag{21}$$

Introducing the operator $\tilde{\mathcal{L}}_A$ which is defined as:

$$\tilde{\mathcal{L}}_A = \left[\frac{1}{2}\frac{\partial^2}{\partial \tilde{y}^2}, \frac{1}{2}\frac{\partial^2}{\partial \tilde{x}^2}, -\frac{\partial^2}{\partial \tilde{x}\partial \tilde{y}}\right] , \tag{22}$$

Eq. 12 can be written in the dimensionless form as:

$$\tilde{\mathcal{L}}_{\mathcal{A}}(\tilde{\boldsymbol{N}}) = \tilde{\kappa}_{xx}\tilde{\kappa}_{yy} - \tilde{\kappa}_{xy}^2 - \tilde{\mathcal{L}}_{\mathcal{A}}(\boldsymbol{E}^{-1}\boldsymbol{A}^{-1}\tilde{\boldsymbol{N}}^{th}\tilde{\tau}) + \tilde{\mathcal{L}}_{\mathcal{A}}(\tilde{\boldsymbol{B}}^{*}\tilde{\boldsymbol{\kappa}}) := \tilde{f}. \tag{23}$$

The in-plane equilibrium equations can be written as:

$$\begin{aligned} \left(\frac{1}{L_x}\tilde{\mathcal{L}}_B(\boldsymbol{A}\boldsymbol{E}\tilde{\boldsymbol{N}}) + \frac{1}{L_y}\tilde{\mathcal{L}}_C(\boldsymbol{A}\boldsymbol{E}\tilde{\boldsymbol{N}})\right) &= 0 \quad \text{on } \tilde{S} \in [-1,1] \\ \tilde{\boldsymbol{N}}.\boldsymbol{n} &= 0 \quad \text{on } \partial\tilde{S} , \end{aligned} \tag{24}$$

where $\tilde{\mathcal{L}}_B$ and $\tilde{\mathcal{L}}_C$ are defined as:

$$\tilde{\mathcal{L}}_B = \begin{bmatrix} \frac{\partial}{\partial \tilde{x}} & 0 & 0 \\ 0 & 0 & \frac{\partial}{\partial \tilde{y}} \end{bmatrix} , \qquad \tilde{\mathcal{L}}_C = \begin{bmatrix} 0 & 0 & \frac{\partial}{\partial \tilde{y}} \\ 0 & \frac{\partial}{\partial \tilde{y}} & 0. \end{bmatrix} \tag{25}$$

From Eq. 23 and Eq. 24, it is possible to write the in-plane stress resultant $\tilde{N}$ in terms of the curvatures $\tilde{\kappa}$ at each point of the DQM grid. Consequently, the strain energy in its non-dimensional form is:

$$\tilde{\Pi} = \int_{-1}^{1}\int_{-1}^{1}\left(\frac{1}{2}\tilde{\boldsymbol{N}}^T\tilde{\boldsymbol{A}}^*\tilde{\boldsymbol{N}} + \frac{1}{2}\tilde{\boldsymbol{\kappa}}^T\tilde{\boldsymbol{D}}^*\tilde{\boldsymbol{\kappa}} - \frac{1}{2}\tilde{\tau}\tilde{\boldsymbol{A}}^{th}\tilde{\tau} - \tilde{\tau}\tilde{\boldsymbol{B}}^{th}\tilde{\boldsymbol{\kappa}} - \tilde{\tau}\tilde{\boldsymbol{D}}^{th}\tilde{\boldsymbol{\kappa}}\right) d\tilde{x}d\tilde{y} , \tag{26}$$

where the non-dimensional material parameters are defined as:

$$\tilde{\boldsymbol{A}}^{*}=\frac{L_xL_y}{\mathit{\Pi}_d}\boldsymbol{E}^T\boldsymbol{A}^*\boldsymbol{E},\quad \tilde{\boldsymbol{B}}^{*}=\boldsymbol{E}^{-1}\boldsymbol{A}^{-1}\boldsymbol{B}\boldsymbol{K},\quad \tilde{\boldsymbol{D}}^{*}=\frac{L_xL_y}{\mathit{\Pi}_d}\boldsymbol{K}^T\tilde{\boldsymbol{D}}^*\boldsymbol{K}$$
$$\tilde{\boldsymbol{A}}^{th}=\frac{L_xL_y}{\mathit{\Pi}_d}\left(\tilde{\boldsymbol{N}}^{th}\right)^T\boldsymbol{A}^*\tilde{\boldsymbol{N}}^{th},\quad \tilde{\boldsymbol{B}}^{th}=\frac{L_xL_y}{\mathit{\Pi}_d}\left(\tilde{\boldsymbol{N}}^{th}\right)^T\boldsymbol{B}^*\boldsymbol{K},\quad \tilde{\boldsymbol{D}}^{th}=\frac{L_xL_y}{\mathit{\Pi}_d}\left(\tilde{\boldsymbol{M}}^{th}\right)^T\boldsymbol{K}\,, \tag{27}$$

and

$$\mathit{\Pi}_d=\mathrm{tr}\left(\begin{bmatrix}\mathbf{E} & \mathbf{0}\\ \mathbf{0} & \mathbf{K}\end{bmatrix}\begin{bmatrix}\mathbf{A} & \mathbf{B}\\ \mathbf{B} & \mathbf{D}\end{bmatrix}\begin{bmatrix}\mathbf{E} & \mathbf{0}\\ \mathbf{0} & \mathbf{K}\end{bmatrix}\right) \tag{28}$$

is a parameter used to scale the total strain energy [15].

4.3. Snap-through

To model the snap-through, the contribution of the external forces must also be added in the virtual work equation as:

$$\delta\tilde{V}=\tilde{F}_z.\delta\tilde{w}\,, \tag{29}$$

where $\tilde{F}_z$ is the non-dimensionalized external force applied at the corners of the bistable plate. The principle of virtual work is written in non-dimensional form as:

$$\delta\tilde{W}_T=\delta\tilde{\mathit{\Pi}}-\delta\tilde{V}=0\,, \tag{30}$$

where $\delta\tilde{W}_T$ is the scaled total virtual work, $\delta\tilde{\mathit{\Pi}}$ is the first variation of the scaled strain energy and $\delta\tilde{V}$ refers to the scaled work done by the applied forces.

The unknowns of the displacement field can be easily found using the Rayleigh-Ritz method. At $\delta\tilde{W}_T=0$, the minimization of the total energy give the stable equilibrium shapes.

$$\frac{\partial\tilde{W}_T(q_{ij})}{\partial q_{ij}}=0\,. \tag{31}$$

This results in a highly nonlinear system of equations (Eq. (31)) which are solved using the Newton-Raphson method. Finally, the stability of the computed equilibrium (stable or unstable) evaluated by means of the construction of the Hessian $\mathbf{H}$, which reads:

$$\mathbf{H}=\frac{\partial^2\tilde{W}_T}{\partial q_{ij}\partial q_{kl}},\ i,j,k,l=0,...,n, \tag{32}$$

where n is the order of the Legendre polynomial. An equilibrium configuration is stable, if and only if the corresponding Hessian matrix (Eq. (32)) is positive definite.

5. DQM formulation

5.1. Differential Quadrature Method

To solve the system of differential equations resulting from the compatibility equation (Eq. 23) and in-plane equilibrium equations (Eq. 24), the Differential Quadrature Method (DQM) [53] is applied in this work. DQM, first presented by Bellmann and Casti [54], is a robust quadrature method where the derivatives of a function at a spatial point are approximated as a weighted sum of all the functional values at the grid points in the entire domain of the variable. This can be applied directly to solve any system of differential equations with boundary conditions. Raju et al. [55] successfully solved the buckling and post-buckling of variable angle tow laminates under in-plane shear loading using DQM, and proved DQM to be an effective tool especially for analyzing simple geometries without any discontinuity. In DQM, the partial derivatives of a function $g(x)$ in matrix form can be written as:

$$\begin{aligned} &\frac{\partial g}{\partial x} = P_x g, \quad \frac{\partial g}{\partial y} = g P_y^T, \quad \frac{\partial^2 g}{\partial x \partial y} = P_x g P_y^T \\ &\frac{\partial^2 g}{\partial^2 x} = Q_x g, \quad \frac{\partial^2 g}{\partial^2 y} = g Q_y^T, \quad \frac{\partial^4 g}{\partial^2 x \partial^2 y} = Q_x g Q_y^T \ , \end{aligned} \tag{33}$$

where P, Q are the DQM coefficients for the first- and second-order partial derivatives with respect to x and y.

A nonlinear grid distribution as given by Chebyshev-Gauss-Lobatto points are used in this work to avoid Runga's phenomenon where oscillations occur at the edges. The grid distribution is given as follows:

$$X_{i,j} = \frac{1}{2}\left[1 - \cos\left(\frac{i-1}{N-1}\pi\right)\right] \ , \tag{34}$$

where i is the number of grid points from 1 to ng_x in the x direction and j is the number of grid point from 1 to ng_y in the y-direction.

The right hand side of Eq. 23 can be written in the expanded form as:

$$
\begin{aligned}
\tilde{f} = {} & \tilde{\kappa}_{xx}\tilde{\kappa}_{yy} - \tilde{\kappa}_{xy}^2 + \frac{1}{2}\Big(\tilde{B}^*_{11}\tilde{\kappa}_{xx,yy} + \tilde{B}^*_{12}\tilde{\kappa}_{yy,yy} + \tilde{B}^*_{13}\tilde{\kappa}_{xy,yy} + \tilde{\kappa}_{xx}\tilde{B}^*_{11,yy} + \tilde{\kappa}_{yy}\tilde{B}^*_{12,yy} \\
& + \tilde{\kappa}_{xy}\tilde{B}^*_{13,yy} + \tilde{B}^*_{21}\tilde{\kappa}_{xx,xx} + \tilde{B}^*_{22}\tilde{\kappa}_{yy,xx} + \tilde{B}^*_{23}\tilde{\kappa}_{xy,xx} + \tilde{\kappa}_{xx}\tilde{B}^*_{21,xx} + \tilde{\kappa}_{yy}\tilde{B}^*_{22,xx} \\
& + \tilde{\kappa}_{xy}\tilde{B}^*_{23,xx}\Big) - \Big(\tilde{B}^*_{31}\tilde{\kappa}_{xx,xy} + \tilde{B}^*_{32}\tilde{\kappa}_{yy,xy} + \tilde{B}^*_{33}\tilde{\kappa}_{xy,xy} + \tilde{\kappa}_{xx}\tilde{B}^*_{31,xy} + \tilde{\kappa}_{yy}\tilde{B}^*_{32,xy} \\
& + \tilde{\kappa}_{xy}\tilde{B}^*_{33,xy}\Big) + \Big(\tilde{B}^*_{11,y}\tilde{\kappa}_{xx,y} + \tilde{B}^*_{12,y}\tilde{\kappa}_{yy,y} + \tilde{B}^*_{13,y}\tilde{\kappa}_{xy,y} + \tilde{B}^*_{21,x}\tilde{\kappa}_{xx,x} + \tilde{B}^*_{22,x}\tilde{\kappa}_{yy,x} \\
& + \tilde{B}^*_{23,x}\tilde{\kappa}_{xy,x} - \tilde{B}^*_{31,x}\tilde{\kappa}_{xx,y} - \tilde{B}^*_{32,x}\tilde{\kappa}_{yy,y} - \tilde{B}^*_{33,x}\tilde{\kappa}_{xy,y} - \tilde{B}^*_{31,y}\tilde{\kappa}_{xx,x} - \tilde{B}^*_{32,y}\tilde{\kappa}_{yy,x} \\
& - \tilde{B}^*_{33,y}\tilde{\kappa}_{xy,x}\Big) - \frac{1}{2}\Big(\mathit{\Gamma}_{11}\tilde{N}^{th}_{xx,yy} + \mathit{\Gamma}_{12}\tilde{N}^{th}_{yy,yy} + \mathit{\Gamma}_{13}\tilde{N}^{th}_{xy,yy} + \tilde{N}^{th}_{xx}\mathit{\Gamma}_{11,yy} + \tilde{N}^{th}_{yy}\mathit{\Gamma}_{12,yy} \\
& + \tilde{N}^{th}_{xy}\mathit{\Gamma}_{13,yy} + \mathit{\Gamma}_{21}\tilde{N}^{th}_{xx,xx} + \mathit{\Gamma}_{22}\tilde{N}^{th}_{yy,xx} + \mathit{\Gamma}_{23}\tilde{N}^{th}_{xy,xx} + \tilde{N}^{th}_{xx}\mathit{\Gamma}_{21,xx} + \tilde{N}^{th}_{yy}\mathit{\Gamma}_{22,xx} \\
& + \tilde{N}^{th}_{xy}\mathit{\Gamma}_{23,xx}\Big) + \Big(\mathit{\Gamma}_{31}\tilde{N}^{th}_{xx,xy} + \mathit{\Gamma}_{32}\tilde{N}^{th}_{yy,xy} + \mathit{\Gamma}_{33}\tilde{N}^{th}_{xy,xy} + \tilde{N}^{th}_{xx}\mathit{\Gamma}_{31,xy} + \tilde{N}^{th}_{yy}\mathit{\Gamma}_{32,xy} \\
& + \tilde{N}^{th}_{xy}\mathit{\Gamma}_{33,xy}\Big) - \Big(\mathit{\Gamma}_{11,y}\tilde{N}^{th}_{xx,y} + \mathit{\Gamma}_{12,y}\tilde{N}^{th}_{yy,y} + \mathit{\Gamma}_{13,y}\tilde{N}^{th}_{xy,y} + \mathit{\Gamma}_{21,x}\tilde{N}^{th}_{xx,x} + \mathit{\Gamma}_{22,x}\tilde{N}^{th}_{yy,x} \\
& + \mathit{\Gamma}_{23,x}\tilde{N}^{th}_{xy,x} - \mathit{\Gamma}_{31,x}\tilde{N}^{th}_{xx,y} - \mathit{\Gamma}_{32,x}\tilde{N}^{th}_{yy,y} - \mathit{\Gamma}_{33,x}\tilde{N}^{th}_{xy,y} - \mathit{\Gamma}_{31,y}\tilde{N}^{th}_{xx,x} - \mathit{\Gamma}_{32,y}\tilde{N}^{th}_{yy,x} \\
& - \mathit{\Gamma}_{33,y}\tilde{N}^{th}_{xy,x}\Big),
\end{aligned}
\tag{35}
$$

where $\boldsymbol{\mathit{\Gamma}} = (\boldsymbol{AE})^{-1}$.

Eq. 35 is a fourth-order elliptic partial differential equation in terms of the out-of-plane displacement w, which is expressed in terms of the curvatures. It also represents the additional terms arising in case of VS laminates. Eq. 35 involves terms containing multiples of the unknown coefficient q_{ij} that are expensive to handle analytically. To increase the computational efficiency, especially for higher order polynomials, a strategy is applied to separate the unknown coefficients from the rest of the expression in Eq. 35. The curvatures $\tilde{\kappa}_{xx}$, $\tilde{\kappa}_{yy}$ and $\tilde{\kappa}_{xy}$ can be rearranged in the form:

$$\tilde{\kappa}_{xx} = \mathbb{K}_x q, \tilde{\kappa}_{yy} = \mathbb{K}_y q, \tilde{\kappa}_{xy} = \mathbb{K}_{xy} q \tag{36}$$

Here, $\mathbb{K}_x$,$\mathbb{K}_y$ and $\mathbb{K}_{xy}$ are the vectorized form of matrices containing the coefficients of q_{ij} for $\tilde{\kappa}_{xx}$, $\tilde{\kappa}_{yy}$ and $\tilde{\kappa}_{xy}$ at each DQM grid point. The vector q refers to the vector containing the parameters q_{ij} as defined in Eq. 20 . By the definition of the curvatures presented in Eq. 36, it is possible to easily separate the unknown terms q_{ij} from its constant coefficient, and therefore avoid involving calculations with unknowns, which ultimately, increases the computationally efficiency.

On the basis of the combination of the unknown coefficients q_{ij}, $\tilde{f}$ can be separated in the following way:

$$\tilde{f} = \mathbf{F_1} q \otimes q + \mathbf{F_2} q + \mathbf{F_3} \, , \tag{37}$$

where $\otimes$ is the Kronecker delta product. Such separation of the variable combination can allow one to avoid symbolic calculations and lead to much faster computations. To systemically depict Eq. 35 in DQM representation, vectorization is performed on all the matrix components. If $\boldsymbol{A}$, $\boldsymbol{B}$, $\boldsymbol{X}$ and $\boldsymbol{C}$ are the given matrices, the equation $\boldsymbol{AXB} = \boldsymbol{C}$ can be written as $\left(\boldsymbol{B}^T \otimes \boldsymbol{A}\right) X = C$. To convert $\mathbf{F_1}$, $\mathbf{F_2}$ and $\mathbf{F_3}$ into the vectorized form, the Kronecker and the Hadamard products are applied to Eq. 35, and can be rearrranged in the form of Eq. 37. The definition of Kronecker Delta product and the Hadamard product can be found in Appendix A. The term $\mathbf{F_1}$ can be written as:

$$\mathbf{F_1} = (\mathbb{K}_x \otimes \mathbb{K}_y - \mathbb{K}_{xy} \otimes \mathbb{K}_{xy}). \tag{38}$$

The above equation can be derived by rearraging the terms of Eq. 35 and writing it in the form of Eq. 37.

The terms $\mathbf{F_2}$ can be written in the vectorized form as:

$$
\begin{aligned}
\mathbf{F_2} = \frac{1}{2} \Bigg(& \left(\vec{B}^*_{11} \otimes \vec{J}\right) \circ (I_y \otimes Q_y)\, \mathbb{K}_x + \left(\vec{B}^*_{12} \otimes \vec{J}\right) \circ (I_y \otimes Q_y)\, \mathbb{K}_y \\
& + \left(\vec{B}^*_{13} \otimes \vec{J}\right) \circ (I_y \otimes Q_y)\, \mathbb{K}_{xy} + \left(\vec{B}^*_{11,yy} \otimes \vec{J}\right) \circ (I_y \otimes \mathbb{K}_x) \\
& + \left(\vec{B}^*_{12,yy} \otimes \vec{J}\right) \circ (I_y \otimes \mathbb{K}_y) + \left(\vec{B}^*_{13,yy} \otimes \vec{J}\right) \circ (I_y \otimes \mathbb{K}_{xy}) \\
& + \left(\vec{B}^*_{21} \otimes \vec{J}\right) \circ (Q_x \otimes I_x)\, \mathbb{K}_x + \left(\vec{B}^*_{22} \otimes \vec{J}\right) \circ (Q_x \otimes I_x)\, \mathbb{K}_y \\
& + \left(\vec{B}^*_{23} \otimes \vec{J}\right) \circ (Q_x \otimes I_x)\, \mathbb{K}_{xy} + \left(\vec{B}^*_{21,xx} \otimes \vec{J}\right) \circ (\mathbb{K}_x \otimes I_x) \\
& + \left(\vec{B}^*_{22,xx} \otimes \vec{J}\right) \circ (\mathbb{K}_y \otimes I_x) + \left(\vec{B}^*_{23,xx} \otimes \vec{J}\right) \circ (\mathbb{K}_{xy} \otimes I_x) \Bigg) \\
& + \Bigg(\left(\vec{B}^*_{11,y} \otimes \vec{J}\right) \circ (I_y \otimes P_y)\, \mathbb{K}_x + \left(\vec{B}^*_{12,y} \otimes \vec{J}\right) \circ (I_y \otimes P_y)\, \mathbb{K}_y \\
& + \left(\vec{B}^*_{13,y} \otimes \vec{J}\right) \circ (I_y \otimes P_y)\, \mathbb{K}_{xy} + \left(\vec{B}^*_{21,x} \otimes \vec{J}\right) \circ (I_y \otimes P_x)\, \mathbb{K}_x \\
& + \left(\vec{B}^*_{22,x} \otimes \vec{J}\right) \circ (I_y \otimes P_x)\, \mathbb{K}_y + \left(\vec{B}^*_{23,x} \otimes \vec{J}\right) \circ (I_y \otimes P_x)\, \mathbb{K}_{xy} \Bigg) \\
& - \Bigg(\left(\vec{B}^*_{31} \otimes \vec{J}\right) \circ (P_x \otimes P_y)\, \mathbb{K}_x + \left(\vec{B}^*_{32} \otimes \vec{J}\right) \circ (P_x \otimes P_y)\, \mathbb{K}_y \\
& + \left(\vec{B}^*_{33} \otimes \vec{J}\right) \circ (P_x \otimes P_y)\, \mathbb{K}_{xy} + \left(\vec{B}^*_{31,xy} \otimes \vec{J}\right) \circ (K_x \otimes I_x) \\
& + \left(\vec{B}^*_{32,xy} \otimes \vec{J}\right) \circ (\mathbb{K}_y \otimes I_x) + \left(\vec{B}^*_{33,xy} \otimes \vec{J}\right) \circ (K_{xy} \otimes I_x) \\
& + \left(\vec{B}^*_{31,x} \otimes \vec{J}\right) \circ (I_y \otimes P_y)\, \mathbb{K}_x + \left(\vec{B}^*_{32,x} \otimes \vec{J}\right) \circ (I_y \otimes P_y)\, \mathbb{K}_y \\
& + \left(\vec{B}^*_{33,x} \otimes \vec{J}\right) \circ (I_y \otimes P_y)\, \mathbb{K}_{xy} + \left(\vec{B}^*_{31,y} \otimes \vec{J}\right) \circ (I_y \otimes P_x)\, \mathbb{K}_x \\
& + \left(\vec{B}^*_{32,y} \otimes \vec{J}\right) \circ (I_y \otimes P_x)\, \mathbb{K}_y + \left(\vec{B}^*_{33,y} \otimes \vec{J}\right) \circ (I_y \otimes P_x)\, \mathbb{K}_{xy} \Bigg) \, , \qquad (39)
\end{aligned}
$$

where $\circ$ is the Hadamard product. The vector $\vec{B}^*_{ij}$ is generated by stacking the components of $\tilde{B}^*$ over the grid points of the two-dimensional domain in a column-wise manner. $\vec{J}$ refers to a row vector defined as: $[1, 1, ..., 1]_{1 \times ng}$, where $ng = ng_x \times ng_y$ representing the total number of grid points. I_x and I_y are identity matrices whose sizes depend on the number of grid points in x and y direction, respectively.

The $\mathbf{F_3}$ matrix does not contain any terms of unknown coefficient q_{ij}, and therefore no vectorization is required.

$$
\begin{aligned}
\mathbf{F_3} = & -\frac{1}{2}\Big(\mathit{\Gamma}_{11}\tilde{N}^{th}_{xx,yy} + \mathit{\Gamma}_{12}\tilde{N}^{th}_{yy,yy} + \mathit{\Gamma}_{13}\tilde{N}^{th}_{xy,yy} + \tilde{N}^{th}_{xx}\mathit{\Gamma}_{11,yy} + \tilde{N}^{th}_{yy}\mathit{\Gamma}_{12,yy} \\
& + \tilde{N}^{th}_{xy}\mathit{\Gamma}_{13,yy} + \mathit{\Gamma}_{21}\tilde{N}^{th}_{xx,xx}\mathit{\Gamma}_{22}\tilde{N}^{th}_{yy,xx} + \mathit{\Gamma}_{23}\tilde{N}^{th}_{xy,xx} + \tilde{N}^{th}_{xx}\mathit{\Gamma}_{21,xx} + \tilde{N}^{th}_{yy}\mathit{\Gamma}_{22,xx} \\
& + \tilde{N}^{th}_{xy}\mathit{\Gamma}_{23,xx}\Big) + \Big(\mathit{\Gamma}_{31}\tilde{N}^{th}_{xx,xy} + \mathit{\Gamma}_{32}\tilde{N}^{th}_{yy,xy} + \mathit{\Gamma}_{33}\tilde{N}^{th}_{xy,xy} + \tilde{N}^{th}_{xx}\mathit{\Gamma}_{31,xy} \\
& + \tilde{N}^{th}_{yy}\mathit{\Gamma}_{32,xy} + \tilde{N}^{th}_{xy}\mathit{\Gamma}_{33,xy}\Big) - \Big(\mathit{\Gamma}_{11,y}\tilde{N}^{th}_{xx,y} + \mathit{\Gamma}_{12,y}\tilde{N}^{th}_{yy,y} + \mathit{\Gamma}_{13,y}\tilde{N}^{th}_{xy,y} \\
& + \mathit{\Gamma}_{21,x}\tilde{N}^{th}_{xx,x} + \mathit{\Gamma}_{22,x}\tilde{N}^{th}_{yy,x} + \mathit{\Gamma}_{23,x}\tilde{N}^{th}_{xy,x} - \mathit{\Gamma}_{31,x}\tilde{N}^{th}_{xx,y} \\
& - \mathit{\Gamma}_{32,x}\tilde{N}^{th}_{yy,y} - \mathit{\Gamma}_{33,x}\tilde{N}^{th}_{xy,y} - \mathit{\Gamma}_{31,y}\tilde{N}^{th}_{xx,x} - \mathit{\Gamma}_{32,y}\tilde{N}^{th}_{yy,x} - \mathit{\Gamma}_{33,y}\tilde{N}^{th}_{xy,x}\Big)\ .
\end{aligned}
\tag{40}
$$

From Eq. 23, the force vector can also be expressed as:

$$
\tilde{N} = \tilde{\mathcal{L}}_{\mathcal{A}}^{-1}\tilde{f} = \quad \widetilde{\mathbf{N}}_{\mathbf{1}} q \otimes q + \widetilde{\mathbf{N}}_{\mathbf{2}} q + \widetilde{\mathbf{N}}_{\mathbf{3}},
\tag{41}
$$

where the introduced coefficient matrices corresponds to:

$$
\widetilde{\mathbf{N}}_{\mathbf{1}} = \tilde{\mathcal{L}}_{\mathcal{A}}^{-1}\left(\mathbf{F_1}\right), \quad \widetilde{\mathbf{N}}_{\mathbf{2}} = \tilde{\mathcal{L}}_{\mathcal{A}}^{-1}\left(\mathbf{F_2}\right), \quad \widetilde{\mathbf{N}}_{\mathbf{3}} \quad = \tilde{\mathcal{L}}_{\mathcal{A}}^{-1}\left(\mathbf{F_3}\right).
\tag{42}
$$

With Eq. 41, the force resultant vector can be written only as a function of unknown coefficients q_{ij} in each DQM point. Therefore, with this approach no additional shape functions are required to describe the in-plane stresses or strains as reported in previous works [56, 15].

5.2. Membrane Energy

The calculated in-plane stress resultants from Eq. 41 can be substituted back into Eq. 26 to calculate the total potential energy. The membrane energy part can be written as:

$$
\tilde{\mathit{\Pi}}_{mem} = \int_{-1}^{1}\int_{-1}^{1}\frac{1}{2}\tilde{\mathbf{N}}^T\tilde{\boldsymbol{A}}^*\tilde{\mathbf{N}}\,d\tilde{x}d\tilde{y}.
\tag{43}
$$

Similar to the differential form, all integration operations on a set of discrete points can be replaced by a matrix multiplication operation. The approach explained by White et al. [57] is adopted in this work to solve the integrals involved in Eq. 43.

In a concise manner, Eq. 43 can be written as:

$$\tilde{\Pi}_{mem} = \mathbf{P}q \otimes q \otimes q \otimes q + \mathbf{Q}q \otimes (q \otimes q) + \mathbf{R}q \otimes q + \mathbf{S}q + \mathbf{T}. \tag{44}$$

Here the coefficients $\mathbf{P}$,$\mathbf{Q}$,$\mathbf{R}$, $\mathbf{S}$ and $\mathbf{T}$ can be correspondingly found from substituting Eq. 41 in Eq. 43. The derived terms of $\mathbf{P}$,$\mathbf{Q}$,$\mathbf{R}$, $\mathbf{S}$ can be found in Appendix B. They can be rearranged and written in terms of the components of the $\tilde{\boldsymbol{A}}^*$ matrix and $\widetilde{\mathbf{N}}_{\mathbf{1}}$, $\widetilde{\mathbf{N}}_{\mathbf{2}}$ and $\widetilde{\mathbf{N}}_{\mathbf{3}}$. The other components of the total strain energy, namely, the bending energy and the energy due to thermal loads can be calculated in a straight-forward manner using Eq. 26. The resultant total energy is a function of unknown coefficients q_{ij}. When external loads are applied, the unknown coefficients q_{ij} are found using Eq. 31 to determine the equilibrium shapes of the laminate.

For the snap-through problem, external loads are applied to one of the stable shape generated from the cool-down process. The contribution of the external load in the total energy is determined using Eq. 29 and Eq. 30. The load is applied incrementally, and therefore only the energy due to external load changes in each increment. The strain energy remains the same and calculations using DQM are only carried out once. The value of the applied force is gradually incremented until snap-through occurs. At each load step, using the Rayleigh-Ritz method all the equilibrium configurations are found. The stability of the equilibrium configurations is found from the Hessian matrix as defined in Eq. 32. Before the limit point is detected, the semi-analytical model produces two stable and one unstable solution. At the limit point where the snap-through occurs, only one unstable solution is observed.

6. Results

In this section, a square laminate with a length L equal to 200 mm, with four layers each of 0.131mm-thick plies of graphite-epoxy prepreg is studied. The plate is subjected to a temperature difference of $\Delta T = -180°$ from curing temperature to room temperature. The material properties at ply-level are given as:

$$\begin{aligned} &E_1 = 161\,\text{GPa},\ E_2 = 11.38\,\text{GPa},\ G_{12} = 5.17\,\text{GPa} \\ &\nu_{12} = 0.3,\ \alpha_1 = -1.8\times10^{-8}/^\circ\text{C},\ \alpha_2 = 3\times10^{-5}/^\circ\text{C}. \end{aligned} \tag{45}$$

In the semi-analytical approach, the membrane problem is solved using a Chebyshev-Lobatto DQ grid of 29×29 nodes. This size of DQ grid is decided based on a convergence study, finding a balance between sufficient accuracy and computational effort. An increasing order of Legendre polynomials is used to describe the out-of-plane displacements.

The investigated VS laminates belong to a family where $\phi = 45^\circ$ and $T_0 + T_1 = 90^\circ$. It was shown in Haldar et al. [12] that this family of VS laminates cools down as a cylindrical shape where the twisting curvature is minimal. This phenomenon occurs due to the fact that the average fiber orientation in the first two layers is 0° and the last two layers is 90° for all VS laminate belonging to this family. Therefore, the laminates satisfying the condition $\phi = 45^\circ$ and $T_0 + T_1 = 90^\circ$ are considered in this study as they yield similar bistable shapes as an unsymmetric cross-ply laminate (Table 1). The work presented by Pirrera et al. [15] is considered as a benchmark for comparison of the results obtained for straight fiber laminates. It was shown previously by Pirrera et al. [15] as well as Diaconu et al. [24] that the snap-through event involves very complex intermediate unstable shapes where higher order polynomial functions are required to capture the snap-through loads accurately. Recently, Groh et al. [58] found further modes near the bifurcation point containing regions of both stable and unstable parts.

In this study, the out-of-plane corner displacement and the snap-through loads are determined using different polynomial orders starting from $n = 2$ to $n = 5$. To verify the semi-analytical model, a nonlinear FE analysis is performed to compare the results using the formulated approach. A total of 96×96 four-node quadrilateral shell elements (S4R) were used in the commercial FE software Abaqus to model the cool-down process from the curing temperature and the snap-through process of VS laminates. The curvilinear fiber path in

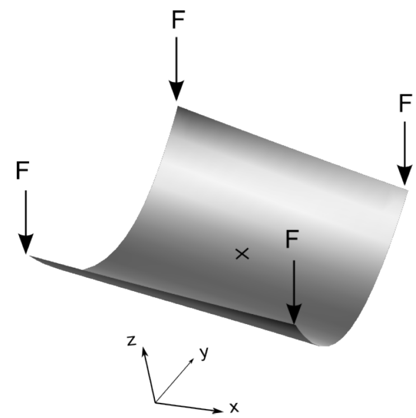

Figure 4: Applied force direction on the bistable plate.

the variable stiffness composite is approximated by using a piecewise function, where each element assumes a straight fiber orientation. The corresponding fiber angle at each element is computed at its centroid from Eq. 1. The chosen mesh proves to have a good approximation of the curvilinear fiber path. Mesh convergence studies show that the adopted mesh size gives sufficiently accurate results, without much change in the results on further mesh refinement.

A linear eigenvalue buckling problem is solved initially under an uniform thermal load on the 'perfect' plate. One of the resulting eigenmodes from the analysis is applied as an imperfection on the actual geometry of the plate. As a

Type	ϕ	T_0	T_1	Layup
Straight	45	45	45	$[0_2/90_2]_T$
VS-1	45	±15	±75	$[45\langle 15\|75\rangle_2/45\langle -15\|-75\rangle_2]_T$
VS-2	45	±30	±60	$[45\langle 30\|60\rangle_2/45\langle -30\|-60\rangle_2]_T$
VS-3	45	±60	±30	$[45\langle 60\|30\rangle_2/45\langle -60\|-30\rangle_2]_T$
VS-4	45	±75	±15	$[45\langle 75\|15\rangle_2/45\langle -75\|-15\rangle_2]_T$

Table 1: Fiber orientation and layup data for the investigated straight cross-ply and various VS laminates

next step, the cool-down process from curing to room temperature is modeled using static FE analysis including geometrical nonlinearities. As the composite plate cools down from curing to room temperature, it warps into one of the stable configurations. The plate is considered to be fixed at the center node during the cool-down process to preclude rigid body motions. Subsequently, external loads are applied equally at the corner of the obtained stable shape. The applied loads and the boundary condition is illustrated in Fig. 4. The loads are applied incrementally in the nonlinear FE framework, and at a particular value, the plate snaps to the other stable shape. Finally, the applied loads are removed so that the plate rests back to the second stable shape. A numerical stabilization is introduced in the form of viscous forces or damping when instabilities are detected both in the cool-down and snap-through process, to facilitate convergence.

The present work is not just concerned in achieving a good correlation with FE, but also rather focuses on understanding how the snap-through loads vary for different VS laminates using a fast and relatively accurate tool, which capture the important physics of the system. The results can be divided particularly into three parts. Four different VS laminate with increasing value of T_0 are investigated and compared with a straight fiber laminate, $[0_2/90_2]$, which can alternatively be written as $T_0 = T_1 = 45°$ and $\phi = 45°$. The layups of the investigated VS laminates are reported in Table 1. In the first part, the corner displacements are reported for the investigated VS laminates and compared with the corresponding FE results. It has also been shown how the accuracy improves with increasing order of Legendre polynomials. In the second part, the in-plane stress resultants solved using DQM are plotted and compared with the corresponding FE results. The load displacement curves are plotted and the snap-through loads are determined for different VS laminates in the third part. Further, a parametric study is conducted in Section 7 where the value of T_0 is incremented by $5°$, with T_1 satisfying $T_1 = 90 - T_0$ and $\phi = 45°$. The tailoring capabilities of the VS laminates are discussed by comparing snap-through loads and the corner displacements.

6.1. Out-of-plane Displacements

The use of VS laminates offers scope to tailor the snap-through loads while retaining the bistable shapes similar to those obtained from unsymmetric cross-ply laminates [59]. Such a wide design space creates opportunities for tailoring the snap-through loads in a way which is not possible using straight fiber laminates. A comprehensive study on how the out-of-plane displacements and curvatures vary with change in the curvilinear fiber orientation is already performed in Haldar et al. [12].

After the cool-down from curing to room temperature, two stable and one unstable solutions are found using the semi-analytical approach described in Section 3, 4 and 5. The corresponding results are compared with the conducted FE analyses. Table 2 shows the initial corner displacement of one of the stable shapes for four different VS laminates. In the table, w_1 and w_2 refers to the adjacent corners. For the studied VS laminates, it is found that the diagonally opposite corners are equal. This is unlike the straight fiber laminate $[0_2/90_2]$ where the out-of-plane displacements at all the corner points are same.

It can be observed that for all cases, the correlation between FE and the analytical results improves as the order of the Legendre polynomials increases. With $n = 5$, the maximum difference between the FE and the analytical results is 4.4% for VS-1, 4.3% for VS-2, 2.9% for VS-3 and 6.9% for VS-4. The corner displacements of the $[0_2/90_2]$ laminate at all the corners are equal.

T_0	T_1	$n=2$		$n=3$		$n=4$		$n=5$		FE	
		w_1	w_2	w_1	w_2	w_1	w_2	w_1	w_2	w_1	w_2
15	75	0.0603	0.0347	0.0502	0.0385	0.0491	0.0381	0.0494	0.0380	0.0481	0.0364
30	60	0.0670	0.0508	0.0643	0.0520	0.0633	0.0510	0.0632	0.0515	0.0608	0.0494
60	30	0.0663	0.0517	0.0658	0.0521	0.0645	0.0502	0.06450	0.0502	0.0627	0.0495
75	15	0.0616	0.0341	0.0531	0.0386	0.0532	0.0341	0.0531	0.0336	0.0497	0.0320

Table 2: Corner displacements: w_1 at $x = L_x/2, y = L_y/2$ and w_2 at $x = -L_x/2, y = L_y/2$ in (m) with increasing polynomial order and $n_x = n_y = 29$.

A comparison on how the stable shapes vary for different VS laminates along the section $x = 0$ is shown in Figure 5. All the VS laminates show cylindrical like stable shape similar to straight fiber $[0_2/90_2]$ laminate. The figure shows a good agreement between FE and the analytical model with $n = 4$, where only at the edges the difference becomes higher, although not more than 1%. A similar graph is also plotted for the orthogonal section $y = 0$ (Figure 6). In this section, it is interesting to observe the difference in the section profile for different VS laminates. The laminates VS-1 and VS-2 exhibit a bulged out surface and VS-3 shows a trench-like profile. On the other hand, the section profile VS-4 at $y = 0$ has both the characteristics of trench and bulged surface. Such undulations in the profile can be due to local differences in the generated residual stresses in the plate due to variation in the material properties at each point of the plate. However, such profile sections can affect how the structures snap-through, as observed previously in Haldar et al. [60].

Although, the magnitudes of the out-of-plane displacements in section $y = 0$ are quite small as compared to section $x = 0$, the differences between semi-analytical and FE results increases appreciably (Figure 6c). The model is less accurate towards the edges, similar to what was observed in the section $x = 0$. However, the nature of the profile in the section $y = 0$ matches well with the FE results, for different VS laminates.

6.2. Determination of the In-Plane Stresses

In the present formulation, it is important that the in-plane stress resultants are calculated accurately, as this affects directly the membrane energy and consequently, the calculation of the snap-through loads. The in-plane stress resultants calculated from the differential equation resulting from the coupled compatibility and the in-plane equilibrium equations (Eq. 12) is found to a have a closed form analytical solution for generic elliptic planform [9]. Hamouche et al. [61] claimed that multiplying the solution from the elliptic planform with a correction factor can provide a sufficiently good estimation of the in-plane stresses and the membrane energy for rectangular shaped plates. The in-plane

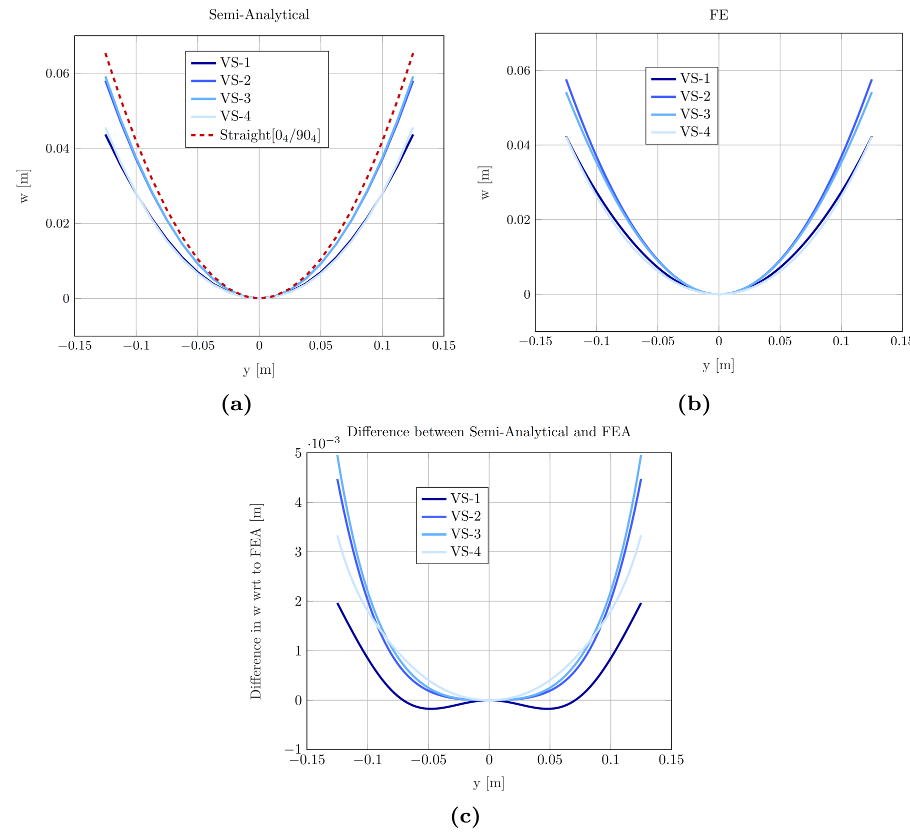

Figure 5: a) Out-of-plane displacement (w) at the section $x = 0$ a) using semi-analytical approach and b) using FE approach c) difference of semi-analytical results with respect to FEA.

stress resultants, as described in Section 4.3, can be calculated by solving the in-plane equilibrium equations and the compatibility equation, which in our case is solved using the aid of DQM. Figure 7 shows the variation of in-plane stress resultants across the plate planform obtained using the formulation described in this paper (left side) and compared with the corresponding FE results (right side) for the VS-3 laminate using a 5^{th} order polynomial. A good correlation is obtained in predicting the in-plane stresses of the laminate. However, due to limited degrees of freedom used in the analytical method, some differences in the maximum and minimum magnitudes can be observed. It is clear from

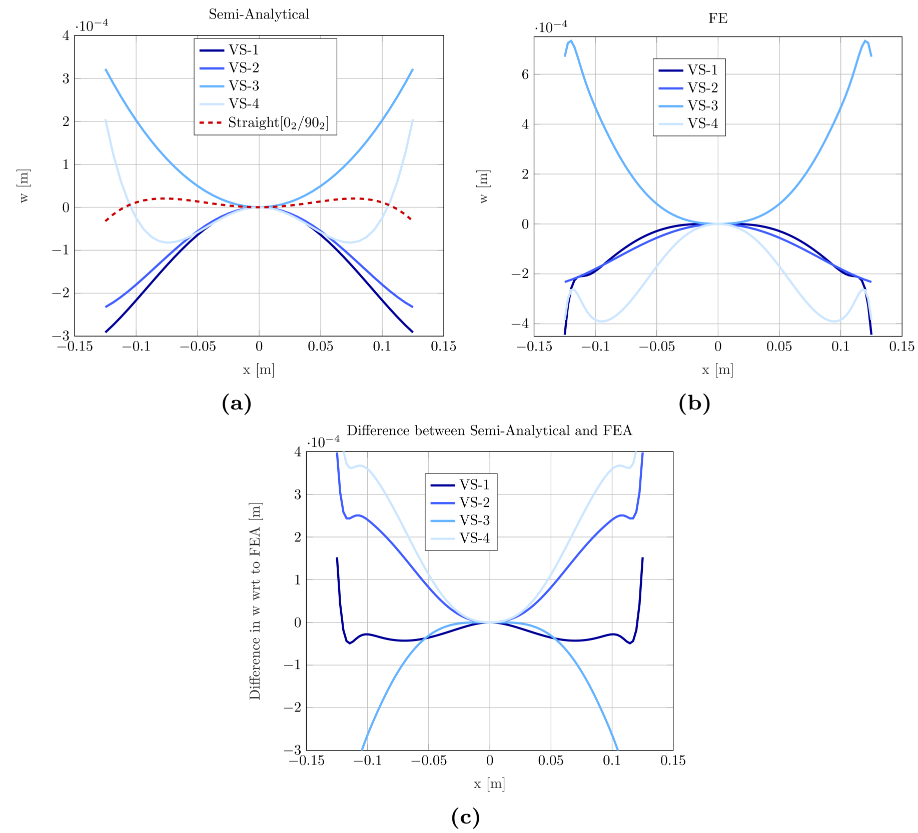

Figure 6: a) Out-of-plane displacement (w) at the section $y = 0$ a) using semi-analytical approach and b) using FE approach c) difference of semi-analytical results with respect to FEA.

Figure 7, where the difference between FE and semi-analytical results is higher at the edges.

6.3. Snap-Through Loads

On one of the obtained stable shapes from the cool-down process, forces in '-z' direction are applied at each corner points (as illustrated in Fig. 4). Like in the cool-down step, the plate is considered to be fixed at the center in this step as well. It has been previously reported [24, 56] that assuming constant curvatures in analytical models can lead to high discrepancies in the calculation of snap-through loads. Similar observations are also reported for VS laminates

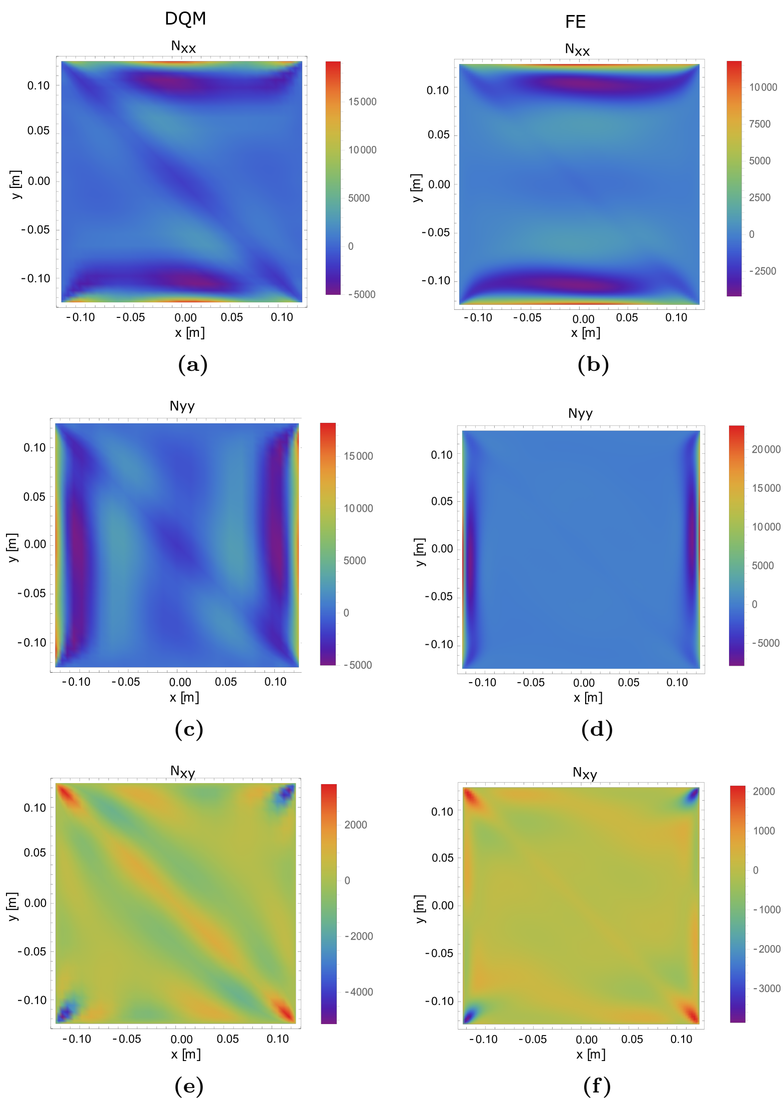

Figure 7: Comparison of the in-plane stress resultants N_{xx},N_{yy} and N_{xy} ($[N/m]$) between DQM (a,c,e) and FE (b,d,f) for VS-3

in Haldar et al. [60]. The snap-through event generally involves intermediate complex shapes and therefore requires a higher-order polynomial function to characterize the shape.

In order to trace the equilibrium path, loads are applied to one of the stable shapes obtained from the cool-down process. Starting from $F = 0N$, the loads at the corner points are incremented until snap-through is detected. These analyses are carried out for different polynomial orders. Table 3 shows the prediction of snap-through loads determined using the semi-analytical model with different polynomial orders and compares with the results obtained from nonlinear FE analyses. It can be noticed that with an increase in the polynomial order, a convergence could be reached. With $n = 5$, a good level accuracy is reached with a difference between FE and analytical results of $4 - 6\%$ for VS laminates.

Figure 8 shows the difference in the snap-through loads by plotting the load-displacement curves of the studied VS laminates. As the load is increased, the limit point is detected where the structure snaps from one stable shape to another. The snap-through load of the cross-ply laminate $[0_2/90_2]$ compares well with the values reported by Lamacchia et al. [27]. It is clear from the figure that changes in the curvilinear fiber configuration can lead to a difference in the snap-through loads. VS-1 shows the lowest snap-through loads, followed by VS-4, VS-2, and VS-3. The constant cross-ply $[0_2/90_2]$ shows the highest snap-through load.

It is observed that laminate VS-2 has 45% lower snap-through force than the straight cross-ply laminate, with just 14% lower out-of-plane displacement. There is thus an immense possibility to tailor the snap-through loads without changing much the shape of the bistable laminate.

To determine the complete load-displacement curve, a nonlinear finite element analysis is conducted in ABAQUS using both static analysis (with stabilization) and the Riks method. The static analysis is equivalent to a force-controlled test, and the Static-Riks corresponds to the arc-length method. Figure 10 shows the load-displacement curve for VS-1 showing "Static-stabilize" in red and "Riks" method in blue. The snap-through forces obtained from both methods compare well with each other. The Riks method shows the complexity of the unstable path attained during the snap-through event. The corresponding equilibrium path was traced using the semi-analytical model. The existence

T_0	T_1	$n = 2$	$n = 3$	$n = 4$	$n = 5$	FE
15	75	1.97	1.91	1.39	1.31	1.23
30	60	3.36	3.24	2.75	2.64	2.46
60	30	6.22	5.56	3.31	3.29	3.17
75	15	4.66	4.20	2.15	1.90	1.79
45	45	4.98	4.32	3.97	3.65	3.35

Table 3: Snap-through loads–in (N) for different VS laminates with increasing order n of Legendre polynomial function and comparison with FE.

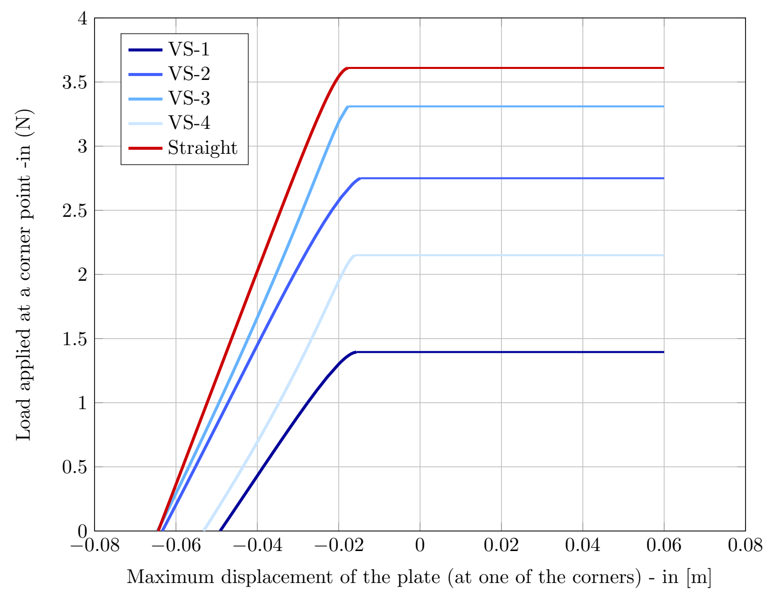

Figure 8: Load-displacement curve from semi-analytical method with $n = 4$ for different VS laminates and straight fiber laminate.

of several unstable equilibria close to each other (as observed in the FE result in Fig. 10) makes it very difficult to trace the unstable path using the adopted semi-analytical approach. Especially for higher orders, where the convergence of roots becomes more sensitive to each parameter of the Legendre polynomial, it can be time-consuming and difficult to determine the unstable path. However, with a 3^{rd} order Legendre polynomial approximation for the out-of-plane

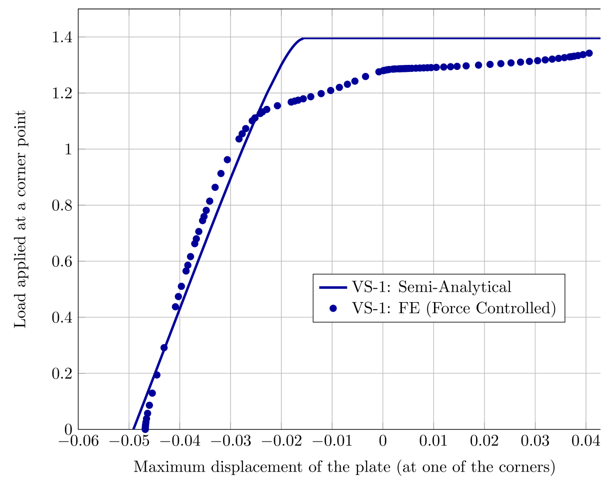

Figure 9: Comparison of the load-displacement curve from semi-analytical results with $n = 4$ and FE results (Static-Stabilize).

displacement, one of the unstable paths could be traced for VS-1. The load-displacement curve for this laminate is shown in Figure 11, where the dotted line represents the unstable path. In contrast to the load-displacement curve found using FEM (Fig. 10), the semi-analytical approach fails to capture the complete unstable path.

The stable equilibrium path, however, is traced within reasonable accuracy. Figure 11 also shows how the equilibrium shape changes at different steps of the load-displacement curve, starting from a stable configuration and leading to the snap-through event, where unstable shapes are illustrated, followed by the second stable shape. At low values of force F, it can be observed from both Fig. 8 and Fig. 11 that the stiffness is found to be linear for all VS laminate. However, in the FE calculation some nonlinearity can be observed in the load-displacement curve as shown in Fig. 9. An Eulerian description incorporated in the semi-analytical method might improve the calculations of the nonlinear regime. In the FE calculations, as the stiffness is updated in every step in an incremental manner, it captures the nonlinear behavior very well. It is also interesting to note that different VS laminates have a different preferential mode of snapping. For example, Figure 12a shows the stable equilibrium shape of VS-1 in the initial state and Figure 12b shows the shape just before snapping. Similarly, the initial stable shape for VS-4 can be seen in Figure 12c and the stable configuration before snapping in Figure 12d. Although the initial shapes of VS-1 and VS-4 (Figure. 12b and Figure. 12c respectively) are similar, both of the laminates snap in different modes. This can be compared with the initial shape and the shape before snapping for the constant stiffness $[0_2/90_2]$ laminate, as illustrated in Figure 12e and Figure 12f respectively, resulting in different snap-through loads. The good agreement of the snapping modes for different VS laminates is found with the FE results (as compared in Fig. 13). It is found that VS-1 and VS-2 showed similar snapping modes (Fig. 13a) and so does VS-3 and VS-4 (Fig. 13c).

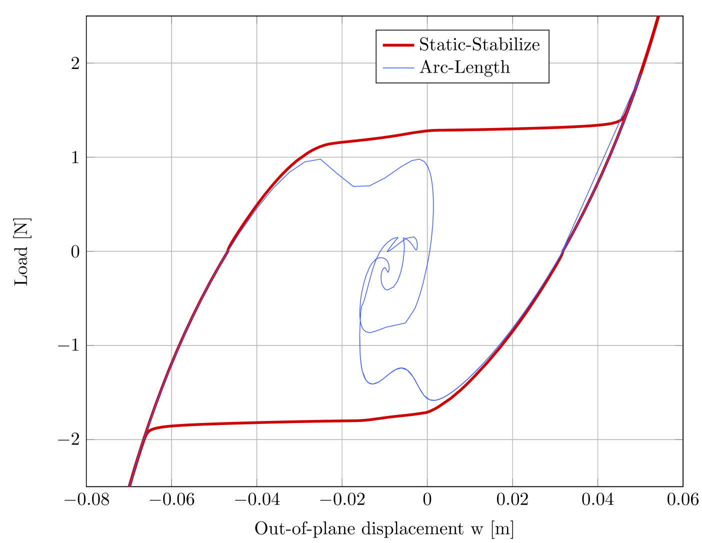

Figure 10: Load-displacement curve obtained for VS-1 using Finite Elements. The curve in red refers to the curve obtained using load-controlled tests (Static-Stabilize) and the curve in blue refers to the curve from the arc-length method (Static-Riks). The load is applied at one of the corner point, and the out-of-plane displacement is recorded at the same point.

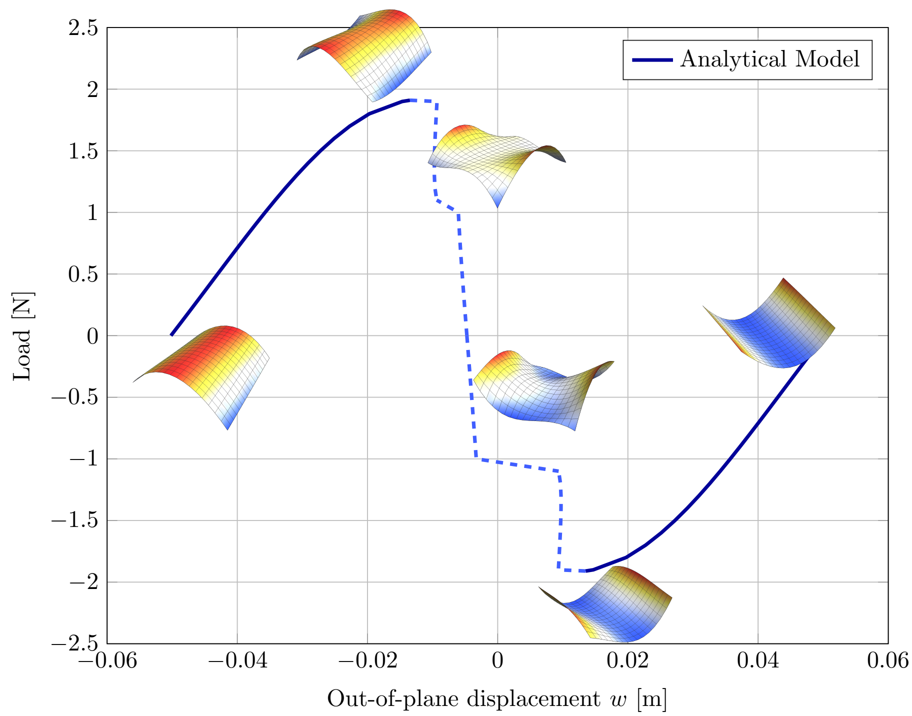

Figure 11: Semi-analytical load-displacement diagram showing the intermediate unstable path for VS-1 with $n = 3$. The load is applied at one of the corner point, and the out-of-plane displacement is recorded at the same point.

7. Parametric Study

As the VS laminate defined for this work depends on three different parameters ϕ, T_0 and T_1, there can be different possibilities to construct VS laminate layups belonging to the family $\phi = 45^\circ$ and $T_0 + T_1 = 90^\circ$. Therefore, a parametric study is required to understand the effect of the VS angle parameters on the corner displacements and the snap-through loads. The main aim of this investigation is to explore VS fiber configurations that have lower snap-through loads but at the same time give higher corner displacements when compared to constant stiffness unsymmetric cross-ply laminates. The same geometry and material property are considered as in Section 6. It must be noted that for this particular family of VS laminate, $\phi = 45^\circ$ and $T_0 = 90^\circ$ corresponds to the

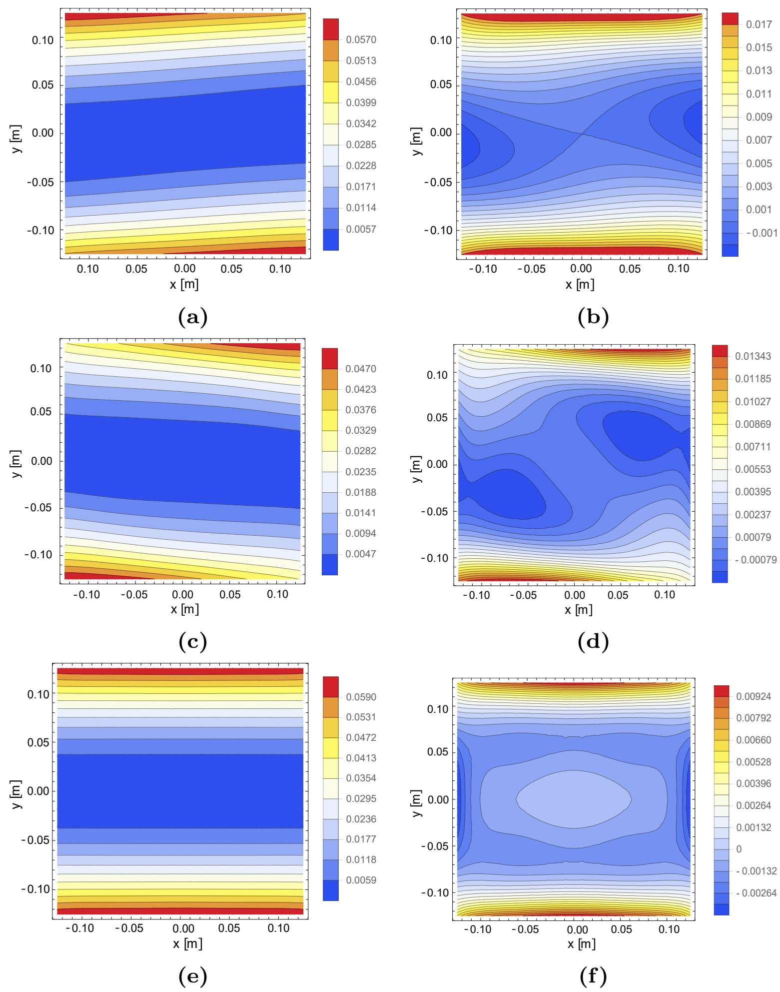

Figure 12: a) Initial contour plot of the bistable plate VS-1 with variable stiffness b) Contour plot just before snap-through event for VS-1 with variable stiffness c) Initial contour plot of the bistable plate VS-4 with variable stiffness d) Contour plot just before snap-through event for VS-4 with variable stiffness e) Initial contour plot of the bistable plate with constant stiffness $[0_2/90_2]$ f) Contour plot just before snap-through event for constant stiffness $[0_2/90_2]$. The contours represent the out-of-plane surface position [m].

straight fiber laminates $[0_2/90_2]$.

A parametric study is conducted where the value of T_0 is incremented by 5°. It can be observed from Figure 14 that certain VS laminates have lower

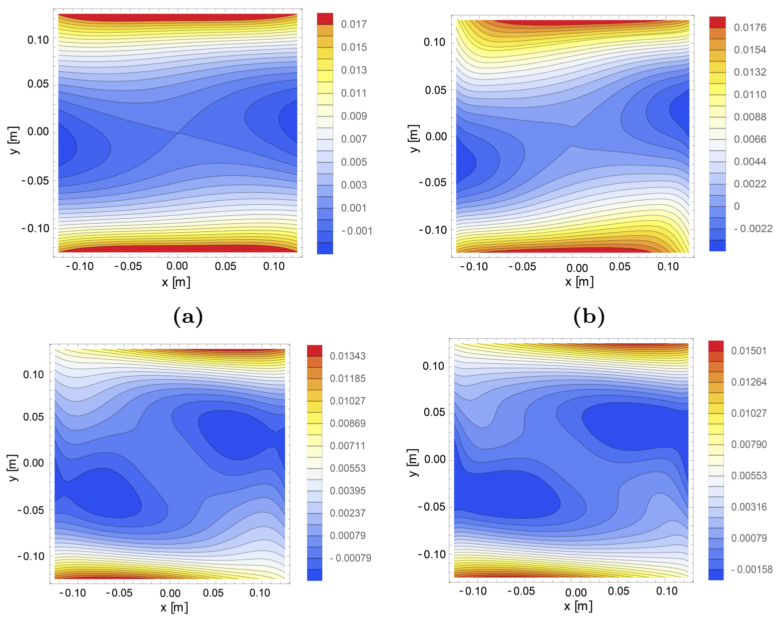

(a) (b) (c) (d)

Figure 13: a) Comparison of snapping modes between the semi-analytical and FE analyses. a) Semi-analytical results for VS-1 b) FE results for VS-1 c) Semi-analytical results for VS-4 b) FE results for VS-4.

snap-through loads but at the same time higher maximum corner displacement than the $[0_2/90_2]$ laminate. Here, the snap-through loads are considered as the total magnitude of forces applied at all the corner points.

For example, improvement in design of a morphing system can be achieved by using a VS laminate with $T_0 = 65°$, where the snap-through loads are 18.65% lower but with 4.1% difference in maximum corner displacement from the constant stiffness $[0_2/90_2]$ laminate.

8. Conclusion

In this paper, the concept of variable stiffness using curvilinear fiber paths was explored to tailor the snap-through loads of bistable laminates. A robust and computationally efficient formulation was derived to calculate the snap-through loads of VS laminates. A strategy is proposed to separate the unknown

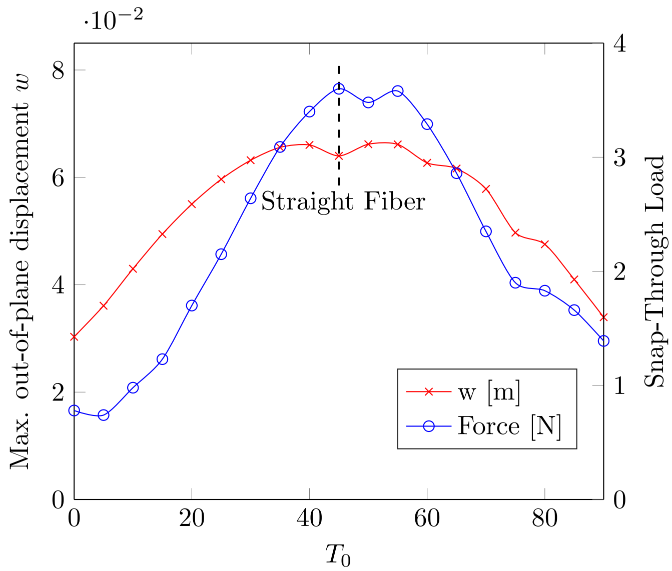

Figure 14: Parametric study performed on the family $\phi = 45°$ and $T_0 + T_1 = 90°$ to investigate the effect of VS angle parameter T_0 on the snap-through loads and the maximum corner displacements.

coefficients of the out-of-plane displacement with the known vectorized terms emanating from the DQM form of the compatibility and in-plane equilibrium differential equations. This process leads to a computationally efficient scheme to determine the snap-through loads. A corresponding FE model was developed to compare the results of the formulated analytical method for a family of VS laminates satisfying $\phi = 45°$ and $T_0 + T_1 = 90°$. This family of VS laminate is chosen as we focus on generating these particular shapes for specific morphing application. Furthermore, the cross-ply straight fiber laminate can be used as a benchmark to quantify the performance of the VS laminates.

The out-of-plane displacement at different sections and at the corner points of four different VS laminates are calculated with the formulated analytical approach and compared with FE results. With increasing order of Legendre polynomials, the comparison with FE results improved. The solutions are then compared with the reference constant stiffness laminate: $[0_2/90_2]$. As the formulation focuses on solving the membrane energy with sufficient accuracy, the in-plane stress resultants solved using the aid of DQM are plotted on the plane of the plate and compared using the in-plane stress resultants btained from the FE results. Different types of undulations were found at the section $x = 0$ for various VS laminates, although a cylindrical profile was observed for all VS laminates at the section $y = 0$. The snap-through loads of the investigated VS laminates are also calculated with increasing orders of Legendre polynomials. At $n = 5$, good convergence is reached with the results obtained from FE analysis. The load-displacement curves are plotted for different VS laminates and the straight fiber laminate. It is observed that laminate VS-2 has 45% lower snap-through force than the straight cross-ply laminate, with just 14% lower out-of-plane displacement. It is interesting to observe that different VS laminates have a different preferential mode of snapping. It is the interplay between the bending and the stretching energies as well the presence of local undulations in the initial stable shape that leads to the difference in the snap-through loads. Some discrepancies between the semi-analytical and FE results are found for in the stable shapes and the snap-through behavior of the different bistable VS laminates. However, with such lower degrees of freedom when compared to FE, the model captures the inherent mechanics of multistable VS laminates in a quite satisfactory manner. The polynomial order can be increased to improve the accuracy, however, this comes at the cost of computational effort due to increased unknowns in the energy term.

The tailoring concept is further explored by conducting a parametric study, where the value of T_0 is incremented by 5° with $T_1 = 90 - T_0$ and $\phi = 45^\circ$. It is observed that with VS laminates, there can be an immense possibility to tailor the snap-through loads without much change in the bistable mode shapes. For example, improvement in the design of a morphing system can be made by using $T_0 = 65^\circ$, where the snap-through loads are lower but with a small difference in the maximum out-of-plane displacement from the constant stiffness $[0_2/90_2]$ laminate. Such snap-through tailoring makes VS laminates a promising alternative to be used in efficient morphing systems. This tool developed in this paper provides a good basis for designers to explore the vast design space available using VS laminates. Full exploitation of the tailoring capabilities shown by VS laminates can be possible by using appropriate optimization tools with this semi-analytical method.

9. Acknowledgement

A. Haldar is grateful to the German Research Foundation (DFG) for funding the research through International Research Training Group 1627. A. Haldar would like to thank Dr. A. Pirrera, Senior Lecturer, Bristol Composites Institute (ACCIS), University of Bristol, Bristol for his valuable comments and discussions. R.M.J. Groh is supported by the Royal Academy of Engineering under the Research Fellowship scheme (Grant No. $RF\backslash 201718\backslash 17178$). P.M. Weaver wishes to thank the Science Foundation Ireland for funding Varicomp (Grant no.:15/RP/2773) under its Research Professor scheme.

Appendix A

If $\boldsymbol{A}$ and $\boldsymbol{B}$ are matrices of size $m\times$n, where $[\mathbf{A}] = a_{ij}$ and $[\mathbf{B}] = b_{ij}$ the Hadamard product is given as:

$$(\mathbf{A} \circ \mathbf{B}) = [a_{ij}b_{ij}] \tag{46}$$

The Kronecker delta product of a matrix $\mathbf{A}$ of size $m \times n$ where $[\mathbf{A}] = a_{ij}$ and matrix $\mathbf{B}$ of size $p \times q$ is defined as:

$$\mathbf{A} \otimes \mathbf{B} = \begin{bmatrix} a_{11}B & \dots & a_{1n}B \\ \vdots & \ddots & \vdots \\ a_{m1}B & & a_{mn}B \end{bmatrix}$$

Appendix B

The value of $\mathbf{P}, \mathbf{Q}, \mathbf{R}, \mathbf{S}$ and $\mathbf{T}$ from Eq. 44 is given as follows:

$$\begin{aligned} \mathbf{P} = \int_{-1}^{1}\int_{-1}^{1} \frac{1}{2} & (A_{11} \circ (N_1)_{xx} \circ (N_1)_{xx} + A_{12} \circ (N_1)_{xx} \circ (N_1)_{yy} + A_{13} \circ (N_1)_{xx} \circ (N_1)_{xy} \\ & + A_{21} \circ (N_1)_{yy} \circ (N_1)_{xx} + A_{22} \circ (N_1)_{x} \circ (N_1)_{xx} + A_{23} \circ (N_1)_{yy} \circ (N_1)_{xy} \\ & + A_{31} \circ (N_1)_{xy} \circ (N_1)_{xx} + A_{32} \circ (N_1)_{xy} \circ (N_1)_{yy} + A_{33} \circ (N_1)_{xy} \circ (N_1)_{xy})\, d\tilde{x} d\tilde{y} \end{aligned} \tag{47}$$

$$\begin{aligned} \mathbf{Q} = \int_{-1}^{1}\int_{-1}^{1} & (A_{11} \circ (N_1)_{xx} \circ (N_2)_{xx} + A_{12} \circ (N_1)_{xx} \circ (N_2)_{yy} + A_{13} \circ (N_1)_{xx} \circ (N_2)_{xy} \\ & + A_{21} \circ (N_1)_{yy} \circ (N_2)_{xx} + A_{22} \circ (N_1)_{yy} \circ (N_2)_{yy} + A_{23} \circ (N_1)_{yy} \circ (N_2)_{xy} \\ & + A_{31} \circ (N_1)_{xy} \circ (N_2)_{xx} + A_{32} \circ (N_1)_{xy} \circ (N_2)_{yy} + A_{33} \circ (N_1)_{xy} \circ (N_2)_{xy})\, d\tilde{x} d\tilde{y} \end{aligned} \tag{48}$$

$$\mathbf{R} = \int_{-1}^{1}\int_{-1}^{1} \frac{1}{2}\left(A_{11} \circ (N_2)_{xx} \circ (N_2)_{xx} + A_{12} \circ (N_2)_{xx} \circ (N_2)_{yy} + A_{13} \circ (N_2)_{xx} \circ (N_2)_{xy}\right.$$
$$+ A_{21} \circ (N_2)_{yy} \circ (N_2)_{xx} + A_{22} \circ (N_2)_{x} \circ (N_2)_{xx} + A_{23} \circ (N_2)_{yy} \circ (N_2)_{xy}$$
$$\left.+A_{31} \circ (N_2)_{xy} \circ (N_2)_{xx} + A_{32} \circ (N_2)_{xy} \circ (N_2)_{yy} + A_{33} \circ (N_2)_{xy} \circ (N_2)_{xy}\right)$$
$$+ \left(A_{11} \circ (N_1)_{xx} \circ (N_3)_{xx} + A_{12} \circ (N_1)_{xx} \circ (N_3)_{yy} + A_{13} \circ (N_1)_{xx} \circ (N_3)_{xy}\right.$$
$$+ A_{21} \circ (N_1)_{yy} \circ (N_3)_{xx} + A_{22} \circ (N_1)_{yy} \circ (N_3)_{yy} + A_{23} \circ (N_1)_{yy} \circ (N_3)_{xy}$$
$$\left.+A_{31} \circ (N_1)_{xy} \circ (N_3)_{xx} + A_{32} \circ (N_1)_{xy} \circ (N_3)_{yy} + A_{33} \circ (N_1)_{xy} \circ (N_3)_{xy}\right) d\tilde{x}d\tilde{y} \tag{49}$$

$$\mathbf{S} = \int_{-1}^{1}\int_{-1}^{1} \left(A_{11} \circ (N_2)_{xx} \circ (N_3)_{xx} + A_{12} \circ (N_2)_{xx} \circ (N_3)_{yy} + A_{13} \circ (N_2)_{xx} \circ (N_3)_{xy}\right.$$
$$+ A_{21} \circ (N_2)_{yy} \circ (N_3)_{xx} + A_{22} \circ (N_2)_{yy} \circ (N_3)_{yy} + A_{23} \circ (N_2)_{yy} \circ (N_3)_{xy}$$
$$\left.+A_{31} \circ (N_2)_{xy} \circ (N_3)_{xx} + A_{32} \circ (N_2)_{xy} \circ (N_3)_{yy} + A_{33} \circ (N_2)_{xy} \circ (N_3)_{xy}\right) d\tilde{x}d\tilde{y} \tag{50}$$

$$\mathbf{T} = \int_{-1}^{1}\int_{-1}^{1} \frac{1}{2}\left(A_{11} \circ (N_3)_{xx} \circ (N_3)_{xx} + A_{12} \circ (N_3)_{xx} \circ (N_3)_{yy} + A_{13} \circ (N_3)_{xx} \circ (N_3)_{xy}\right.$$
$$+ A_{21} \circ (N_3)_{yy} \circ (N_3)_{xx} + A_{22} \circ (N_3)_{x} \circ (N_3)_{xx} + A_{23} \circ (N_3)_{yy} \circ (N_3)_{xy}$$
$$\left.+A_{31} \circ (N_3)_{xy} \circ (N_3)_{xx} + A_{32} \circ (N_3)_{xy} \circ (N_3)_{yy} + A_{33} \circ (N_3)_{xy} \circ (N_3)_{xy}\right) d\tilde{x}d\tilde{y} \tag{51}$$

References

[1] M. R. Schultz, A Concept for Airfoil-like Active Bistable Twisting Structures, Journal of Intelligent Material Systems and Structures 19 (2) (2007) 157–169 (2007).

[2] F. Mattioni, P. M. Weaver, K. D. Potter, M. I. Friswell, The application of thermally induced multistable composites to morphing aircraft structures, in: The 15th International Symposium on: Smart Structures and Materials

& Nondestructive Evaluation and Health Monitoring, International Society for Optics and Photonics, 2008, pp. 693012–693012 (2008).

[3] A. F. Arrieta, I. K. Kuder, T. Waeber, P. Ermanni, Variable stiffness characteristics of embeddable multi-stable composites, Composites Science and Technology 97 (2014) 12–18 (jun 2014).

[4] S. Daynes, S. Nall, P. Weaver, K. Potter, P. Margaris, P. Mellor, On a Bistable Flap for an Airfoil, in: 50th AIAA/ASME/ASCE/AHS/ASC Structures, Structural Dynamics, and Materials Conference, Structures, Structural Dynamics, and Materials and Co-located Conferences, American Institute of Aeronautics and Astronautics, 2009 (May 2009).

[5] C. G. Diaconu, P. M. Weaver, F. Mattioni, Concepts for morphing airfoil sections using bi-stable laminated composite structures, Thin-Walled Structures 46 (6) (2008) 689–701 (Jun. 2008).

[6] F. Nicassio, G. Scarselli, F. Pinto, F. Ciampa, O. Iervolino, M. Meo, Low energy actuation technique of bistable composites for aircraft morphing, Aerospace Science and Technology 75 (2018) 35 – 46 (2018).

[7] A. Haldar, E. Jansen, R. Rolfes, Analysis of morphing trailing edge flap with embedded multistable variable stiffness laminates, in: AIAA Scitech 2019 Forum, 2019, p. 0856 (2019). `doi:10.2514/6.2019-0856`.

[8] M. W. Hyer, Some Observations on the Cured Shape of Thin Unsymmetric Laminates, Journal of Composite Materials 15 (2) (1981) 175–194 (1981).

[9] K. Seffen, 'morphing' bistable orthotropic elliptical shallow shells, Proceedings of the Royal Society of London A: Mathematical, Physical and Engineering Sciences 463 (2077) (2007) 67–83 (2007).

[10] Y. Yang, M. A. Dias, D. P. Holmes, Multistable kirigami for tunable architected materials, Physical Review Materials 2 (11) (2018) 110601 (2018).

[11] S. Daynes, C. Diaconu, K. Potter, P. Weaver, Bistable prestressed symmetric laminates, Journal of Composite Materials 44 (9) (2010) 1119–1137 (2010).

[12] A. Haldar, J. Reinoso, E. Jansen, R. Rolfes, Thermally induced multistable configurations of variable stiffness composite plates: Semi-analytical and finite element investigation, Composite Structures 183 (2018) 161 – 175, in honor of Prof. Y. Narita (2018).

[13] A. S. Panesar, P. M. Weaver, Optimisation of blended bistable laminates for a morphing flap, Composite Structures 94 (10) (2012) 3092–3105 (Oct. 2012).

[14] A. S. Panesar, K. Hazra, P. M. Weaver, Investigation of thermally induced bistable behaviour for tow-steered laminates, Composites Part A: Applied Science and Manufacturing 43 (6) (2012) 926 – 934 (2012).

[15] A. Pirrera, D. Avitabile, P. M. Weaver, Bistable plates for morphing structures: A refined analytical approach with high-order polynomials, International Journal of Solids and Structures 47 (25-26) (2010) 3412–3425 (2010).

[16] M.-L. Dano, M. W. Hyer, the Response of Unsymmetric Laminates To Simple Applied Forces, Mechanics of Advanced Materials and Structures 3 (1) (1996) 65–80 (1996).

[17] M. R. Schultz, W. K. Wilkie, R. G. Bryant, Investigation of self-resetting active multistable laminates, Journal of aircraft 44 (4) (2007) 1069–1076 (2007).

[18] E. Loukaides, S. Smoukov, K. Seffen, Magnetic actuation and transition shapes of a bistable spherical cap, International Journal of Smart and Nano Materials 5 (4) (2014) 270–282 (2014).

[19] K. A. Seffen, S. Vidoli, Eversion of bistable shells under magnetic actuation: a model of nonlinear shapes, Smart Materials and Structures 25 (6) (2016) 065010 (2016).

[20] D. P. Holmes, M. Roché, T. Sinha, H. A. Stone, Bending and twisting of soft materials by non-homogenous swelling, Soft Matter 7 (2011) 5188–5193 (2011).

[21] M. Pezzulla, N. Stoop, X. Jiang, D. P. Holmes, Curvature-driven morphing of non-euclidean shells, Proceedings of the Royal Society of London A: Mathematical, Physical and Engineering Sciences 473 (2201) (2017).

[22] J.-G. Lee, J. Ryu, S.-W. Kim, J.-S. Koh, K.-J. Cho, M. Cho, Effect of initial tool-plate curvature on snap-through load of unsymmetric laminated cross-ply bistable composites, Composite Structures 122 (2015) 82 – 91 (2015).

[23] R. Groh, A. Pirrera, Orthotropy as a driver for complex stability phenomena in cylindrical shell structures, Composite Structures 198 (2018) 63 – 72 (2018).

[24] C. G. Diaconu, P. M. Weaver, A. F. Arrieta, Dynamic analysis of bi-stable composite plates, Journal of Sound and Vibration 322 (4–5) (2009) 987 – 1004 (2009).

[25] K. Potter, P. Weaver, A. A. Seman, S. Shah, Phenomena in the bifurcation of unsymmetric composite plates, Composites Part A: Applied Science and Manufacturing 38 (1) (2007) 100 – 106 (2007).

[26] F. Mattioni, P. M. Weaver, M. Friswell, Multistable composite plates with piecewise variation of lay-up in the planform, International Journal of Solids and Structures 46 (1) (2009) 151–164 (Jan. 2009).

[27] E. Lamacchia, A. Pirrera, I. Chenchiah, P. Weaver, Morphing shell structures: A generalised modelling approach, Composite Structures 131 (2015) 1017 – 1027 (2015).

[28] S. Vidoli, International Journal of Solids and Structures Discrete approximations of the Föppl – Von Kármán shell model : From coarse to more refined models, International Journal of Solids and Structures 50 (9) (2013) 1241–1252 (2013).

[29] A. Haldar, E. Jansen, R. Rolfes, P. Weaver, Tailoring snap-through loads in variable stiffness composites, in: 2018 AIAA/ASCE/AHS/ASC Structures, Structural Dynamics, and Materials Conference, 2018, p. 2245 (2018). doi:10.2514/6.2018-2245.

[30] H. A. Kim, D. N. Betts, A. I. T. Salo, C. R. Bowen, Shape memory alloy-piezoelectric active structures for reversible actuation of bistable composites, AIAA Journal 48 (6) (2010) 1265–1268 (2010).

[31] K. C. Wu, Thermal and Structural Performance of Tow-Placed, Variable Stiffness Panels, IOS Press, 2006 (2006).

[32] G. G. Lozano, A. Tiwari, C. Turner, S. Astwood, A review on design for manufacture of variable stiffness composite laminates, Proceedings of the Institution of Mechanical Engineers, Part B: Journal of Engineering Manufacture 230 (6) (2016) 981–992 (2016).

[33] A. Spickenheuer, M. Schulz, K. Gliesche, G. Heinrich, Using tailored fibre placement technology for stress adapted design of composite structures, Plastics, Rubber and Composites 37 (5) (2008) 227–232 (2008).

[34] M. Hyer, H. Lee, The use of curvilinear fiber format to improve buckling resistance of composite plates with central circular holes, Composite Structures 18 (3) (1991) 239 – 261 (1991).

[35] M. W. Hyer, R. F. Charette, Use of curvilinear fiber format in composite structure design, AIAA Journal 29 (1991) 1011–1015 (Jun. 1991).

[36] Z. Gurdal, R. Olmedo, In-plane response of laminates with spatially varying fiber orientations-variable stiffness concept, AIAA journal 31 (4) (1993) 751–758 (1993).

[37] Z. Gurdal, B. Tatting, K. Wu, Tow-Placement Technology and Fabrication Issues for Laminated Composite Structures, in: 46th

AIAA/ASME/ASCE/AHS/ASC Structures, Structural Dynamics and Materials Conference, Structures, Structural Dynamics, and Materials and Co-located Conferences, American Institute of Aeronautics and Astronautics, 2005 (Apr 2005).

[38] Z. Wu, G. Raju, P. M. Weaver, Postbuckling analysis of variable angle tow composite plates, International Journal of Solids and Structures 50 (10) (2013) 1770 – 1780 (2013).

[39] B. H. Coburn, Z. Wu, P. M. Weaver, Buckling analysis of stiffened variable angle tow panels, Composite Structures 111 (2014) 259 – 270 (2014).

[40] T. A. Guimarães, D. A. Rade, C. E. Cesnik, Active flutter suppression on composite tow steered panels based on piezoelectric actuation, in: 2018 AIAA/ASCE/AHS/ASC Structures, Structural Dynamics, and Materials Conference, 2018, p. 0188 (2018).

[41] L. Parnas, S. Oral, Ümit Ceyhan, Optimum design of composite structures with curved fiber courses, Composites Science and Technology 63 (7) (2003) 1071 – 1082 (2003).

[42] S. Nagendra, S. Kodiyalam, J. Davis, V. Parthasarathy, Optimization of tow fiber paths for composite design, in: 36th Structures, Structural Dynamics and Materials Conference, 1995, p. 1275 (1995).

[43] M. Montemurro, A. Catapano, On the effective integration of manufacturability constraints within the multi-scale methodology for designing variable angle-tow laminates, Composite Structures 161 (2017) 145 – 159 (2017).

[44] A. Alhajahmad, M. M. Abdalla, Z. Gürdal, Design tailoring for pressure pillowing using tow-placed steered fibers, Journal of Aircraft 45 (2) (2008) 630–640 (2008).

[45] S. Setoodeh, A. Blom, M. Abdalla, Z. Gürdal, Generating Curvilinear Fiber Paths from Lamination Parameters Distribution, in: 47th

AIAA/ASME/ASCE/AHS/ASC Structures, Structural Dynamics, and Materials Conference, Structures, Structural Dynamics, and Materials and Co-located Conferences, American Institute of Aeronautics and Astronautics, 2006 (May 2006).

[46] T. R. Brooks, J. R. Martins, On manufacturing constraints for tow-steered composite design optimization, Composite Structures 204 (2018) 548 – 559 (2018).

[47] D. M. Peeters, G. G. Lozano, M. M. Abdalla, Effect of steering limit constraints on the performance of variable stiffness laminates, Computers & Structures 196 (2018) 94 – 111 (2018).

[48] G. G. Lozano, A. Tiwari, C. Turner, A design algorithm to model fibre paths for manufacturing of structurally optimised composite laminates, Composite Structures 204 (2018) 882 – 895 (2018).

[49] Z. Gürdal, B. Tatting, C. Wu, Variable stiffness composite panels: Effects of stiffness variation on the in-plane and buckling response, Composites Part A: Applied Science and Manufacturing 39 (5) (2008) 911–922 (May 2008).

[50] R. M. Jones, Mechanics of Composite Materials, Mc Graw Hill, New York, 1975 (1975).

[51] E. H. Mansfield, The inextensional theory for thin flat plates, Quarterly Journal of Mechanics and Applied Mathematics 8 (3) (1955) 338–352 (1955).

[52] C. Calladine, The theory of thin shell structures 1888–1988, Proceedings of the Institution of Mechanical Engineers, Part A: Journal of Power and Energy 202 (3) (1988) 141–149 (1988).

[53] C. Shu, Differential Quadrature and Its Application in Engineering, Springer-Verlag, London, 2000 (2000).

[54] R. Bellman, J. Casti, Differential quadrature and long-term integration, Journal of Mathematical Analysis and Applications 34 (2) (1971) 235 – 238 (1971).

[55] G. Raju, Z. Wu, P. M. Weaver, Buckling and postbuckling of variable angle tow composite plates under in-plane shear loading, International Journal of Solids and Structures 58 (2015) 270 – 287 (2015).

[56] M.-L. Dano, M. W. Hyer, Snap-through of unsymmetric fiber-reinforced composite laminates, International Journal of Solids and Structures 39 (1) (2002) 175–198 (2002).

[57] S. White, G. Raju, P. Weaver, Initial post-buckling of variable-stiffness curved panels, Journal of the Mechanics and Physics of Solids 71 (2014) 132 – 155 (2014).

[58] R. Groh, D. Avitabile, A. Pirrera, Generalised path-following for well-behaved nonlinear structures, Computer Methods in Applied Mechanics and Engineering 331 (2018) 394 – 426 (2018).

[59] P. M. Anilkumar, A. Haldar, E. Jansen, B. N. Rao, R. Rolfes, Design optimization of multistable variable-stiffness laminates, Mechanics of Advanced Materials and Structures 26 (1) (2019) 48–55 (2019).

[60] A. Haldar, J. Reinoso, E. Jansen, R. Rolfes, Snap-Through of Bistable Configurations Generated from Variable Stiffness Composites, Springer International Publishing, Cham, 2018, pp. 61–82 (2018).

[61] W. Hamouche, C. Maurini, A. Vincenti, S. Vidoli, Basic criteria to design and produce multistable shells, Meccanica (2016).